Identification of Probe of an Atomic Force Microscope Using Curve Fitting

S. Rajagopal

Master of Science Thesis

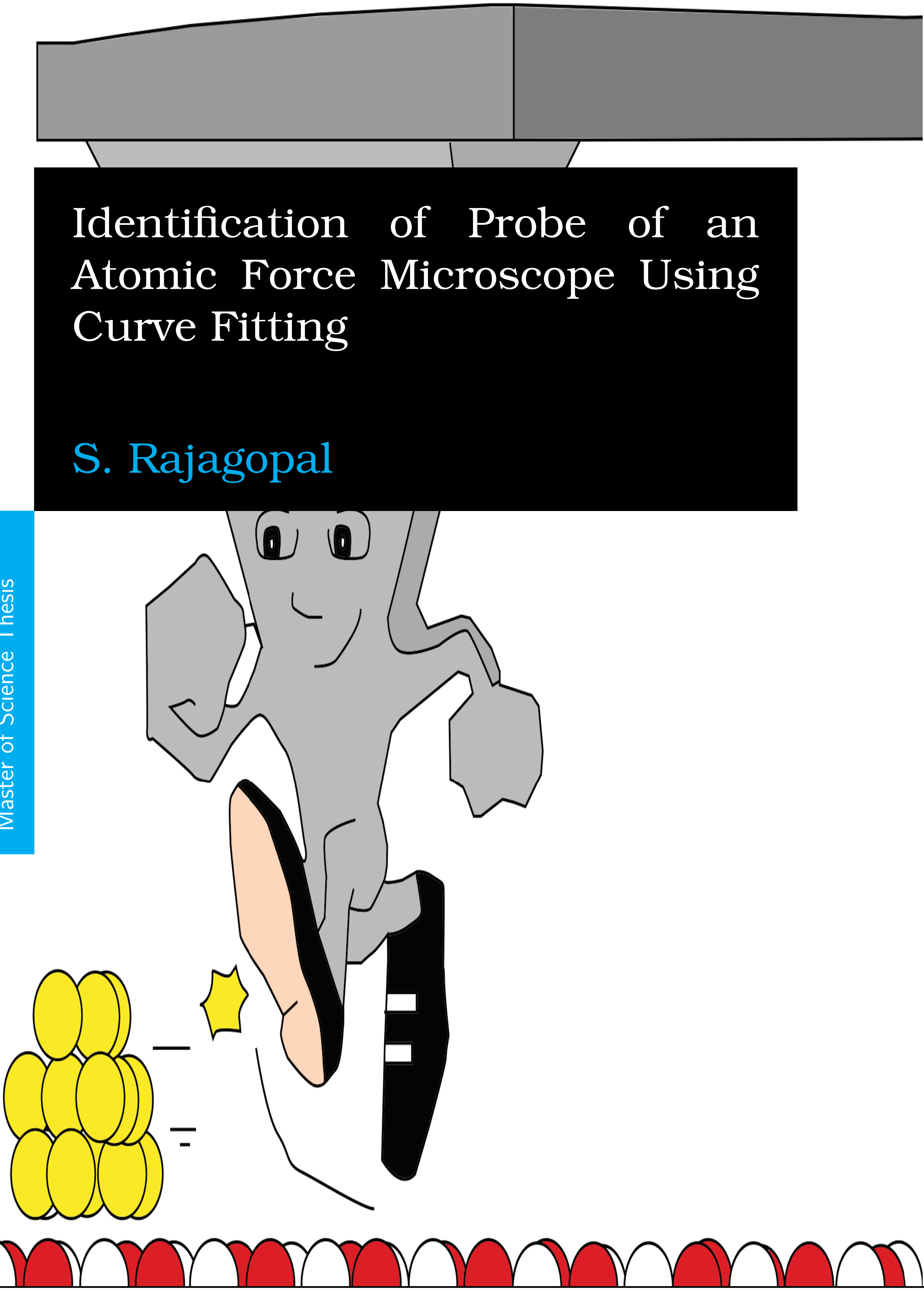

Delft Center for Systems and Control

Identification of Probe of an Atomic Force Microscope Using Curve Fitting

Master of Science Thesis

For the degree of Master of Science in Systems and Control at Delft University of Technology

S. Rajagopal

August 24, 2017

Faculty of Mechanical, Maritime and Materials Engineering (3mE) · Delft University of Technology

The work in this thesis was supported by TNO. Their cooperation is hereby gratefully acknowledged.

DELFT UNIVERSITY OF TECHNOLOGY
DEPARTMENT OF
DELFT CENTER FOR SYSTEMS AND CONTROL (DCSC)

The undersigned hereby certify that they have read and recommend to the Faculty of Mechanical, Maritime and Materials Engineering (3mE) for acceptance a thesis entitled

IDENTIFICATION OF PROBE OF AN ATOMIC FORCE MICROSCOPE USING CURVE FITTING

by

S. RAJAGOPAL

in partial fulfillment of the requirements for the degree of

MASTER OF SCIENCE SYSTEMS AND CONTROL

Dated: August 24, 2017

Supervisor(s): prof.dr.ir.Jan Willem van Wingerden

A. Keyvani Janbahan

Reader(s): dr. Hassan HosseinNia

Preface

This document presents a detailed report of my master thesis on Identification of the probe of an Atomic Force Microscope. The ultimate aim of this thesis is to estimate a mathematical model for the probe of an atomic force microscope and hence use it to determine tip-sample forces with better accuracy. The thesis report details the algorithm developed to determine a mathematical model for an AFM probe. The results obtained by applying the developed algorithm to simulated and experimental data are included in the report.

I would like to thank my supervisors dr. ir. J.W. van Wingerden and A.Keyvani Janbahan for giving me this opportunity to research in the field of system identification. I would also like to thank Mehmet Selman Tamer who helped me with the experiments on the Bruker system. I would also take this opportunity to thank everyone at TNO who helped me progress whenever I had problems understanding concepts. I also thankfully acknowledge the contributions of Bhavna Thyagarajan in helping me create clear and good looking images.

Finally, my deep and sincere gratitude to my family and friends who have continuously supported me throughout this journey. They selflessly encouraged me during this journey and it would not have been possible without their love and support.

Delft, University of Technology S. Rajagopal
August 24, 2017

"I think anything is possible if you have the mindset and the will and desire to do it and put the time in"

–Roger Clemens

Abstract

In recent years the Tapping Mode-Atomic Force Microscope (TM-AFM) has become one of the most important tools for imaging on the nanometer scale. In comparison with other contemporary technologies, the AFMs have been able to obtain atomic resolution both in high vacuum and liquid environments thus affirming their supremacy. The AFM can be perceived as a combination of a mechanical profilometer, where mechanical springs are used to sense the forces, and a Scanning tunneling microscope, where piezo-electric transducers are used for scanning. The AFM is widely used to generate a topographical image of the sample surface and also to study certain characteristics of the sample. The latter is aided by measuring the forces between the sample surface and the tip of the probe.

The non-linear, rapidly changing and hysteretic behavior of the tip-sample forces makes their accurate estimation extremely difficult in dynamic AFM. Moreover, the cantilever probe responds to an average of the different forces acting on the probe tip. Since several permutations of different forces can give the same periodic average, the accurate estimation of each of these forces has been evidently impossible. However, some probes exist for which the motion of the cantilever consists of super harmonic components of the tip-sample forces which provide more information about the tip-sample forces. Nevertheless the construction of these cantilevers is challenging and time consuming. Knowledge of the dynamic properties of the cantilever facilitates one to study its behaviour to a particular input. Since different forces act at different tip sample distances, a more mathematical approach towards tip-sample force estimation which includes the dynamic characteristics of the cantilever is necessary.

The accurate knowledge of the cantilever dynamics is extremely important for precise estimation of tip-sample forces, deduction of mechanical properties, controller synthesis etc. Therefore in this research, the techniques to identify the state space matrices is explored. One, rather old but an immensely useful identification method are the black box identification techniques. These techniques can be used to accurately estimate the fully parameterized state space matrices of the system. The main difficulty arises in estimating these parameters specially in the absence of one of the inputs (tip-sample interactions).

In this thesis research, an algorithm is developed to identify the fully parameterized state space matrices. A secondary cantilever of very high fundamental resonance frequency is used as a force sensor. This force sensor set up along with the periodic property of the tip-sample forces during TM-AFM is used to reconstruct the tip-sample interaction forces. Using the estimated tip-sample forces, a transfer function between the cantilever deflection and the estimated force is identified using a curve fitting technique. The curve fitting technique uses iterative least squares to reduce the two norm between the experimental frequency response and the frequency response estimated using the identified transfer function.

Table of Contents

1 Introduction **1**

2 Atomic Force Microscope **5**

2-1 Working principle 6

2-2 Problems- Accurate estimation of the tip-sample forces 10

2-3 Problem Statement 11

3 Frequency Domain Identification **13**

3-1 Experimental set-up 13

3-2 Estimation of Tip-Sample Interactions 14

3-3 Signal Averaging and Noise Floor 18

3-4 Transfer Function Estimation for the Imaging cantilever 18

4 Simulation and Experimental Results **23**

4-1 Results from Simulation 23

4-2 Results from Experimental Data 34

5 Conclusions **49**

A Optical Beam Deflection Method **51**

B Lock-in Amplifier **53**

C Signal Averaging **55**

Bibliography **57**

List of Figures

1-1 (*Top*) Motion of the cantilever in TM-AFM. Instance ① represents the moment when the attractive forces exceed the stiffness of cantilever, ② is the instance of maximum indentation where the sample experiences peak repulsive force and ③ is the instance where the retract motion of the cantilever overcomes the adhesive force between cantilever tip and sample surface. (*Bottom*) Figure represents the tip-sample force during one cycle of cantilever oscillations. Forces at corresponding instances as the figure on top are represented in the figure. 2

2-1 Atomic resolution image of graphene obtained using an AFM. 6

2-2 Block Diagram of the set up of an AFM. 6

2-3 Schematic diagram of an AFM- depicting the working principle in detail. 8

2-4 Force-distance curve in an AFM. 9

2-5 Schematic of feedback control for amplitude modulation. 9

2-6 Freqeuncy response of a cantilever, depicting band pass characteristics. 10

2-7 Cantilever block diagram with the different inputs and outputs. 12

3-1 Experimental set-up as suggested in [1]. 14

3-2 Represent of the Experimental Set-Up using blocks. 15

4-1 (Top) Simulated deflection of imaging cantilever. (Bottom) Steady state part of the imaging cantilever deflection. 25

4-2 Magnitude plot of the imaging cantilever (Zoomed into first bending mode). . . 26

4-3 FFT of Deflection of Sensing Cantilever ($F_{tapping} = 39850Hz$). 27

4-4 FFT of Assumed Tip-sample interactions ($F_{tapping} = 39850Hz$). 28

4-5 Assumed and Estimated Tip-sample interactions ($F_{tapping} = 39850Hz$). 29

4-6 Comparison of bode plots of the Assumed(Blue) and Estimated Transfer Function(Red). 30

4-7 Comparison of bode plots of the Estimated(Blue) and Assumed Transfer Function(Red)[Estimated with one Data]. 30

4-8 Plot of poles and zeros of the estimated system for 10 iterations. 31

4-9 Plot of poles of the estimated system for 10 iterations (zoomed). 32

4-10 Comparison of Bode plot of the estimated system at different noise level. 33

4-11 Comparison of Bode plot of the estimated system at noise of 10dB. 33

4-12 Comparison of Bode plot of the estimated transfer between deflection signal and the dithering signal using PI-MOESP. 34

4-13 Schematic representation of a dynamically tuned cantilever. 35

4-14 First resonance peak obtained through thermal fluctuations. 36

4-15 Movement of the Imaging Cantilever with z-stage movement. 37

4-16 Movement of the Imaging Cantilever with z-stage movement (T-B signal). 38

4-17 Movement of the Sensing cantilever with z-stage movement. 38

4-18 Movement of the Sensing cantilever with z-stage movement. 39

4-19 Power Spectrum of Deflection of Sensing Cantilever (52033 Hz). 39

4-20 Power Spectrum of Deflection of Sensing Cantilever (52090 Hz). 40

4-21 Power Spectrum of Deflection of Sensing Cantilever (52847 Hz). 40

4-22 Estimated Tip-Sample Interactions at 52033 Hz and 52090 Hz. 41

4-23 Estimated Tip-Sample Interactions at 52847 Hz. 42

4-25 Comparison between estimated tip-sample interaction using proposed method and force sensitivity method ($F_{tapping} = 52847Hz$). 42

4-24 Estimated Tip-Sample Interactions superimposed with the corresponding deflection signal (52090 Hz) 43

4-26 Frequency Spectrum of Deflection of Imaging cantilever ($f_{tapping} = 52033Hz$) . 44

4-27 Frequency Spectrum of Deflection of Imaging cantilever ($f_{tapping} = 52090Hz$) . 44

4-28 Frequency Spectrum of Deflection of Imaging cantilever ($f_{tapping} = 52847Hz$) . 45

4-29 Bode plot of the Estimated system with magnitude of frequency response as weighting matrix. 46

4-30 Bode plot of the Estimated system with weighting matrix $W(\omega_k)$. 47

4-31 Thermal tune of second bending mode of imaging cantilever. 48

A-1 Schematic of the optical beam deflection method. 51

B-1 Block diagram of a simple lock-in amplifier. 53

Chapter 1

Introduction

The Atomic Force Microscope (AFM) is well known for measurement and surface manipulation of sample in the nanometer scale. Recent advances in the field of AFMs has increased its application to beyond topography imaging, such as nano-mechanical property mapping [2], thermal conductivity mapping [3] and much more. A number of surface characteristics like the adhesion strength [4], sample stiffness [5] and surface potential can be studied from the accurate estimation of the forces between the cantilever tip of an AFM and the sample surface. There have been techniques in the past that aim at estimating these tip-sample forces by either introducing secondary excitation signals [6, 7, 8] or alter the geometry of the cantilever to excite higher bending modes [9, 10]. These methods have been successful in exciting the higher eigenmodes of an AFM cantilever thus obtaining more information about the tip-sample forces. However some critical information is lost due to the band pass characteristics of the cantilever. A special Kalman filter [11] tries to estimate the tip-sample forces as the states of a linear time invariant (LTI) system but the knowledge of the dynamics of cantilever is necessary to design such linear filters. Thus the accurate estimation of tip-sample interactions is still an open research.

Figure 1-1 depicts one period of tip-sample force curve in tapping mode AFM during approach and retract of the cantilever probe tip. When the probe tip approaches the sample surface, the attractive forces namely van der Waals forces and electrostatic forces pull the tip towards the surface. At point 1, the negative attractive forces exceed the cantilever's stiffness and pull the probe tip into the sample surface. The tip indents into the sample surface till it reaches its maximum point (point 2) after which the probe starts withdrawing until it reaches the "pull off" point (point 3). At this point the repulsive forces become greater in magnitude than the adhesion forces and hence decouple from the sample surface. Critical information about peak force, magnitude of attractive forces, repulsive forces and adhesive forces can then be retrieved from the tip-sample force signal. Thus, accurate estimation of the tip-sample forces is extremely important to study different surface characteristics of the sample.

Including the dynamics of higher bending modes of the cantilever leads to more accurate

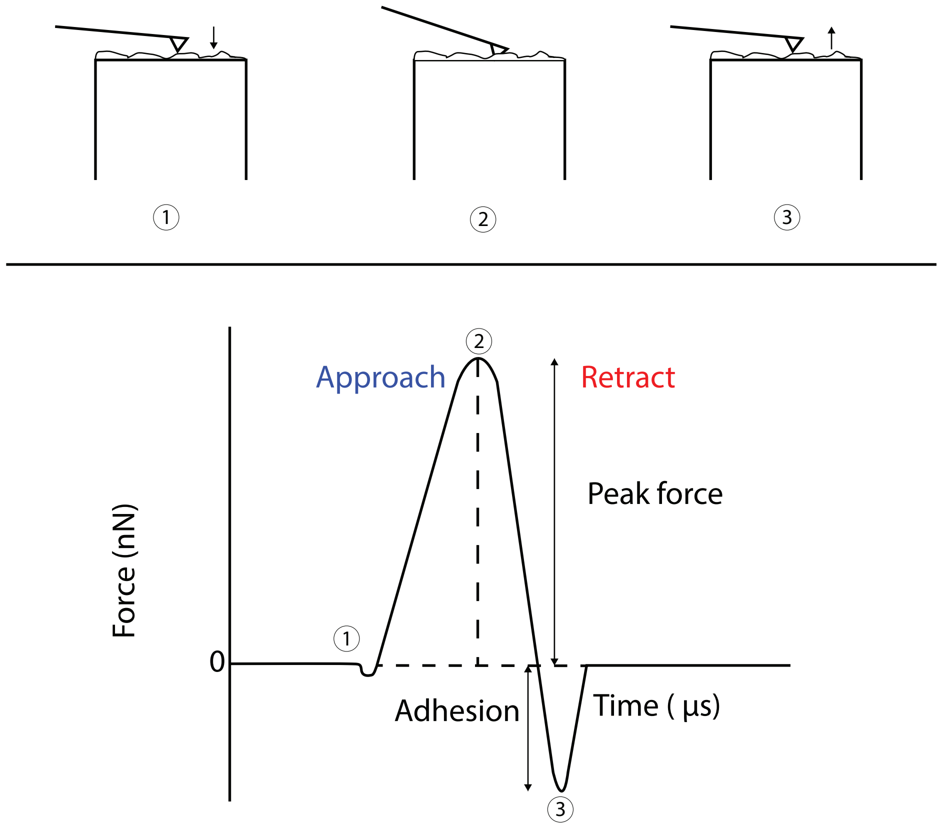

Figure 1-1: (*Top*) Motion of the cantilever in TM-AFM. Instance ① represents the moment when the attractive forces exceed the stiffness of cantilever, ② is the instance of maximum indentation where the sample experiences peak repulsive force and ③ is the instance where the retract motion of the cantilever overcomes the adhesive force between cantilever tip and sample surface.

(*Bottom*) Figure represents the tip-sample force during one cycle of cantilever oscillations. Forces at corresponding instances as the figure on top are represented in the figure.

estimation of the tip-sample interactions[11]. The dynamics of any LTI system can be represented through a state space notation. AFM cantilevers possess number of eigenmodes each with its own natural frequency. To model the dynamics of the cantilever, it can be considered as a rectangular beam [12]. Thus, the dynamics of each of the eigen modes can be represented through the following second order differential equation

$$m\ddot{x}_i + c\dot{x}_i + kx_i = F(t)$$

with m being the modal mass, c being the modal damping coefficient and k the modal spring constant. From physical considerations these modal parameters are required to be positive. The variable F(t) is the net force applied and $x_i(t)$ is the displacement of the individual bending mode of the cantilever. With the choice of $z(t) = \begin{bmatrix} x_i(t) & \dot{x}_i(t) \end{bmatrix}^T$ as the states of the system, the state space representation of the above equation is given by

$$\dot{z}(t) = \begin{bmatrix} 0 & 1 \\ \frac{-k}{m} & \frac{-c}{m} \end{bmatrix} z(t) + \begin{bmatrix} 0 \\ \frac{1}{m} \end{bmatrix} F(t)$$
$$y(t) = \begin{bmatrix} 1 & 0 \end{bmatrix} z(t)$$

Discretization of the above state space system using a **Zero Order Hold (ZOH)** technique yields a fully parameterized state space representation. Thanks to the subspace identification techniques [13, 14, 15], the identification of fully parameterized state space representation has been an easy problem. Although the identification of these state space matrices in the presence of an unknown input is still in its nascent stages. Blind Identification techniques are such identification techniques [16, 17, 18] that estimate the state space matrices in the presence of unknown inputs. The essence of these methods lies in the exploitation of the prior knowledge about the system and statistical properties of the inputs. With the failure of traditional unknown input estimation techniques to AFM probe identification in Tapping Mode-AFM (TM-AFM), a different algorithm needs to be developed.

Thus, the ultimate goal of the thesis project is to develop an algorithm to obtain a fully parameterized state space representation that will facilitate model based controller design and also help in estimating the tip-sample forces with improved accuracy.

This thesis report provides an algorithm to obtain a mathematical model for an AFM probe. The algorithm is discussed in detail, the advantages and drawbacks of the algorithm are explored and future recommendations are provided. The algorithm is tested on simulated data, as well as on experimental data obtained using Bruker Atomic Force Microscope.

The report is organized as follows :

Chapter 2 introduces the reader to the basics of atomic force microscopy which includes the components of an AFM and its basic working principle. It introduces the reader to TM-AFM and the various methods available to estimate the tip-sample forces. The chapter concludes by providing the problem statement for the thesis.

Chapter 3 provides the reader with methodology used in the thesis project to obtain a mathematical model for the AFM probe in detail. Tip-sample estimation and curve fitting method are also elaborately discussed.

Chapter 4 presents the reader with the results of the algorithm being applied to simulated data as well as experimental data. The algorithm is tested for several noise levels and the results are analyzed in detail.

Chapter 5 provides important conclusions about the implemented algorithm and also suggests recommendations to improve the estimation process.

Chapter 2

Atomic Force Microscope

Atomic-force microscopy or scanning force microscopy is a form of scanning probe microscopy with resolutions of the order of fractions of nanometer. The AFM can be perceived as a combination of mechanical profilometer, where springs are used to sense forces, and scanning tunneling microscope (STM), where piezoelectric transducers are used for scanning [19].

The main functionalities of an AFM include topography imaging, force measurement and surface property manipulation [20]. Information for these tasks is obtained by either “feeling” or “touching” the sample surface. For imaging the topography of the surface, the reaction of the probe to the forces between the probe tip and sample surface is used to create a 3-D image of the sample surface. A method called raster-scanning is used for this purpose, where the probe is moved horizontally across the sample surface and then in its perpendicular direction thus scanning the entire length of the sample surface [21]. While scanning the surface it is ensured that the distance between the probe-tip and the sample surface is kept constant and the images are created using the feedback control signal used to keep the distance constant as the probe is raster scanned.

AFM is also used for force-spectroscopy [22]. The nature of forces between the atoms of the sample (van der Waals, adhesive forces etc) are studied by finding the accurate tip-sample interaction forces. Generally the probe is assumed to obey Hooke’s Law and the forces thus measured are a linear function of deflection of the cantilever that is measured [23][24].

For the manipulation task the force between the tip of the AFM and sample surface is used to change the properties of sample in a controlled way. Manipulation is generally used in lithography, atomic manipulation and local stimulation of cells. Simultaneously, while generating the 3-D images of the sample surface, other properties of the sample surface can also be measured locally and represented as an image. Mechanical properties like stiffness, adhesion strength and electrical properties like surface potential and conductivity can be studied. Figure 2-1 represents an atomic resolution image of graphene using an AFM. The honeycomb structure of graphene is clearly visible proving the superiority and possibilities of an AFM.

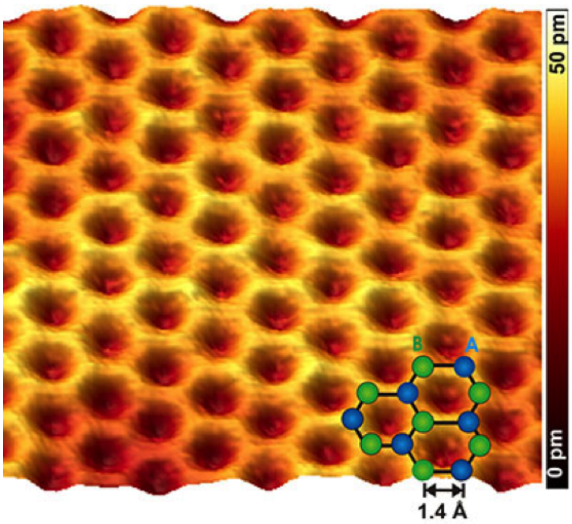

Figure 2-1: Atomic resolution image of graphene obtained using an AFM.

Source : http://www.nanoscience.de/HTML/research/graphene.html

2-1 Working principle

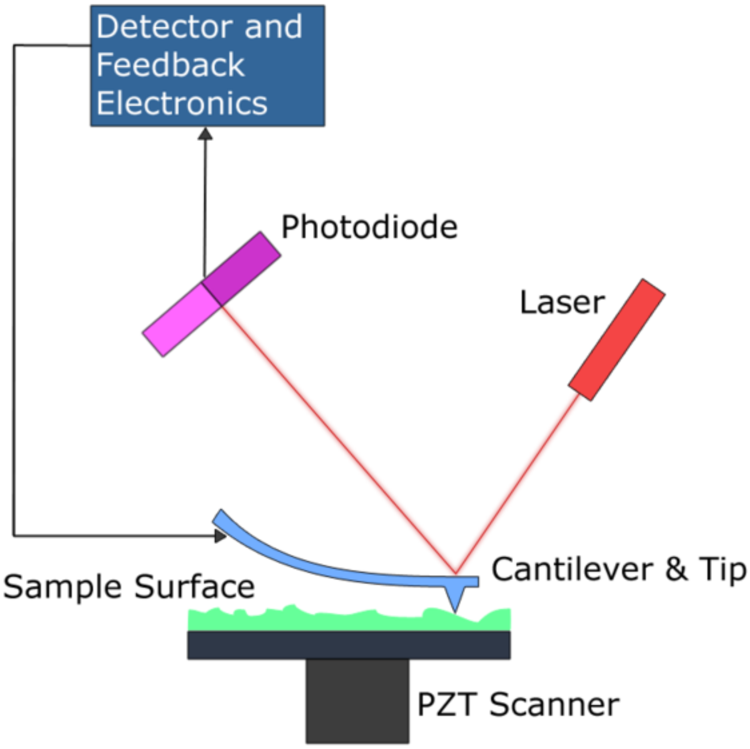

Figure 2-2: Block Diagram of the set up of an AFM.

Figure 2-2 gives a schematic representation of an AFM. An AFM typically consists of the following five essential components [25]

- A sharp tip (probe) mounted on a soft spring like cantilever.
- A way of sensing the deflection of cantilever (photo-diode+laser).
- A feedback control system to monitor and control the cantilever deflection (detector and feedback electronics).
- A mechanical scanning system, usually a piezoelectric actuator, that is used to move the mounted sample with respect to the tip in a raster pattern (represented as PZT in Figure 2-2).
- A display system that converts the acquired data into a 3-D image.

The cantilever is held to its position using a rigid support and a piezoelectric element is used to dither the cantilever at a particular frequency. The sample is mounted on a sample stage, which is mounted on a xyz drive made of a piezoelectric material. This enables the movement of the sample stage in all directions in accordance to the feedback received from the controller.

The AFM can be operated in various modes but tapping mode atomic fore microscope (TM-AFM) is the most widely used operating mode for topography imaging. Hence for this thesis TM-AFM is considered and only TM-AFM will be discussed further. The working principle and the industrial applications of other modes of operation can be found in [26].

Tapping mode of imaging was developed to overcome the problem of the tip sticking to the sample surface during non-contact mode. Every sample tends to develop a thin layer liquid meniscus in ambient conditions which causes the stickiness of the surface [27]. In tapping mode (intermittent contact mode) the cantilever tip is made to oscillate at or near its natural frequency, touching the sample surface at every oscillation. The energy possessed by the tip is enough to prevent the tip from sticking to the sample surface. In general stiff cantilevers, with high spring constant and high Quality factor are used to overcome the tip sticking to the sample surface. At each oscillation when the tip comes in close proximity to the sample surface, it experiences attractive and repulsive forces thus causing the amplitude to change. The deflection sensor measures the deflection of the cantilever from its reference amplitude and it is ensured through a feedback controller that the amplitude of oscillation of the cantilever is maintained at a pre-determined value. This mode is advantageous when compared to the contact mode because the lateral forces on the sample surface are essentially removed. This can be attributed to the fact that the tip is in contact with the sample surface for a brief period of time and it is not dragged along the surface while imaging [27].

Figure 2-3 depicts the detailed working mechanism of an TM-AFM. The cantilever is dithered at a pre determined constant amplitude using a piezoelectric material at its fundamental resonance frequency (which depends on the dimensions of the cantilever and its material of construction).

When the probe tip approaches the sample surface, the long range attractive forces, namely van der Waals forces, electrostatic forcs etc. are dominant and the tip is pulled towards the sample surface until it is in complete contact with the surface. From this instant, the

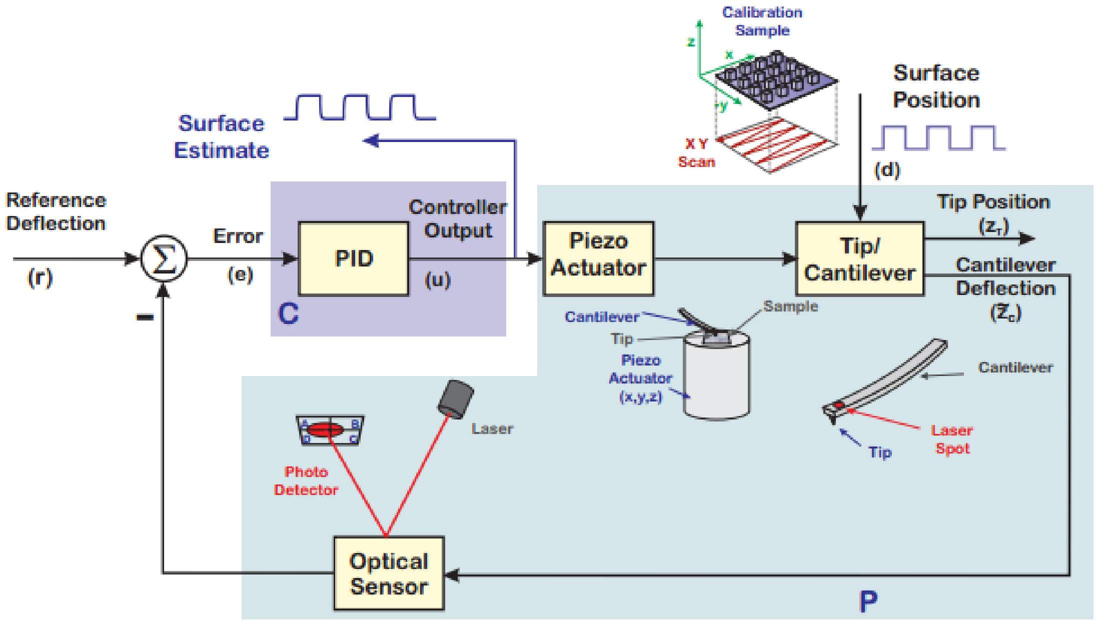

Figure 2-3: Schematic diagram of an AFM- depicting the working principle in detail.

Source : A tutorial on the mechanisms, dynamics, and control of atomic force microscopes [28].

repulsive forces start dominating thus deflecting the probe tip. Depending on the amount of deflection of the cantilever oscillation, the sample stage is moved in the z (vertical) direction to maintain the amplitude of oscillation of the tip at the pre-determined value. This makes the choice of the tip amplitude a very critical decision to ensure that the tip leaves the surface of the sample (mainly while dealing with aqueous surfaces)[29]. A typical force vs distance curve is shown in Figure (2-4) where the blue part depicts the region where attractive forces are dominant and the red part depicts the region of dominance of the repulsive forces.

The repulsive and attractive forces between the tip and the sample surface cause the cantilever to deflect by a small amount, which can be measured using a deflection sensor. These deflection sensors can be any sensor that can measure a change in the amplitude of oscillation such as electron tunneling, interferometry, capacitance methods and beam deflection. Owing to its simplicity, optical beam deflection (OBD) methods are most commonly used for this purpose.

Once the deflection is measured using one of the above mentioned methods, the feedback controller electronics provide the necessary control input to move the xyz stage in order to maintain the tip amplitude at the pre determined value. The control signal is then broken down into amplitude and phase using a lock-in amplifier. The amplitude and phase signals are further interpreted to create a topographical image of the sample surface. The xyz stage has three degrees of freedom i.e it can move along the three mutually perpendicular directions. The stage is moved in the z-direction to maintain the tip amplitude at a constant value and along the x-y plane to raster scan the complete sample surface. Detailed working principle of

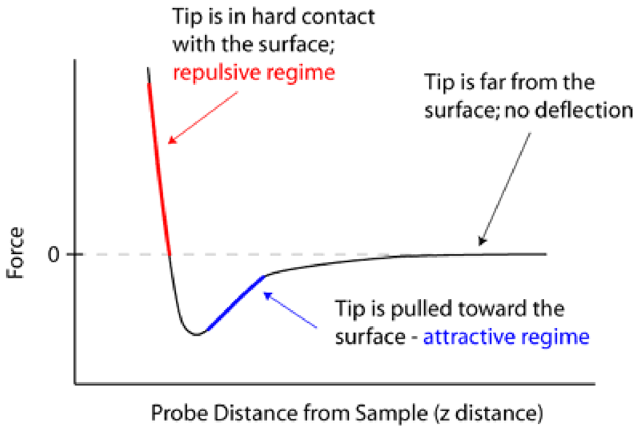

Figure 2-4: Force-distance curve in an AFM.

OBD method and lock-in amplifier can be found in the **Appendix**.

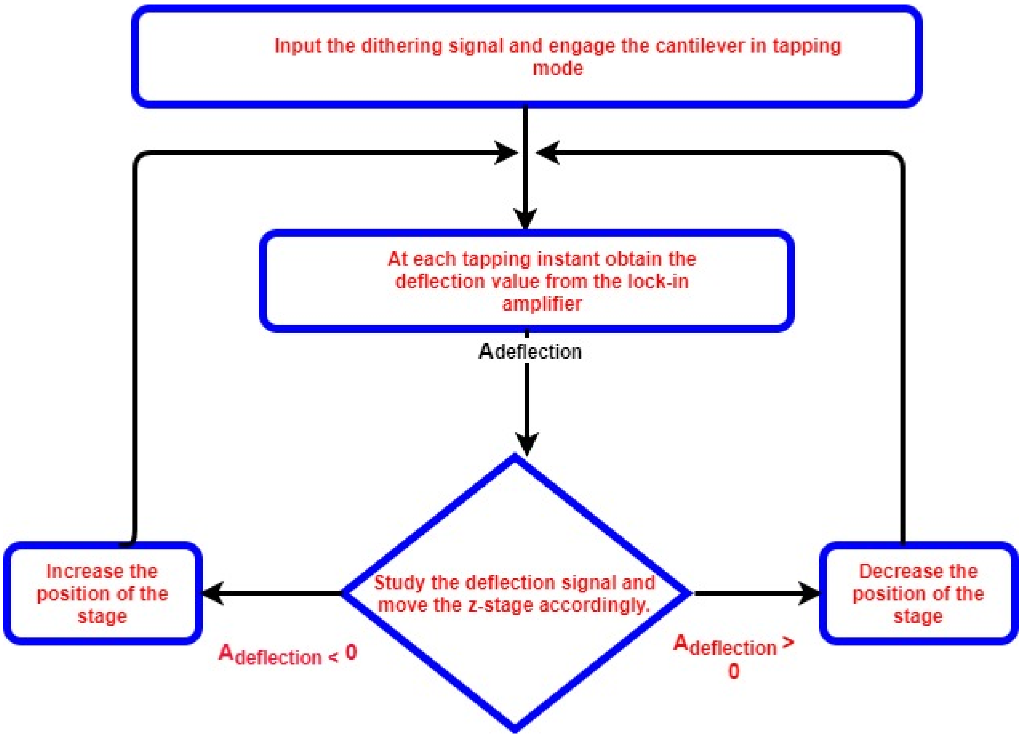

Figure 2-5: Schematic of feedback control for amplitude modulation.

Figure 2-5 depicts the feedback control strategy adapted by the feedback electronics in TM-AFM. In the figure $A_{deflection}$ is the deflection obtained from the OBD and lock in amplifier combination. Whenever the deflection sensor perceives an increase in the deflection the controller signals the xyz stage to move closer to the tip and when the deflection sensor perceives a reduction in deflection the controller signals the xyz stage to move away from the tip thus maintaining the tip amplitude.

2-2 Problems- Accurate estimation of the tip-sample forces

The harmonic motion of the cantilever in TM-AFM has made the accurate estimation of the tip-sample interactions seemingly impossible. This can be attributed to the fact that a commercially available cantilever shows band pass characteristics. Figure 2-6 represents a typical magnitude response of a cantilever. The cantilever is seen to allow frequencies close to its resonance frequencies to pass through and has high attenuation at other frequencies. Since in TM-AFM the cantilever is dithered at close to its resonance frequency, the higher harmonics present in the tip-sample forces do not manifest themselves in the observable cantilever deflection signal.

Also, the resonance frequencies of higher bending modes of majority of commercially available cantilevers are not integral multiples of the fundamental resonance frequency. Thus the higher harmonics of the tip-sample interactions are very low in magnitude and hence are unobservable in the deflection signal of the cantilever. Earlier tip-sample force estimation methods estimate the forces as scaled values of the deflection signal, scaling factor being the effective stiffness of the cantilever. This linear relation is valid only when higher bending modes are not excited. Thus when higher bending modes are excited, the knowledge of modal stiffness constants is necessary to estimate the tip-sample interactions.

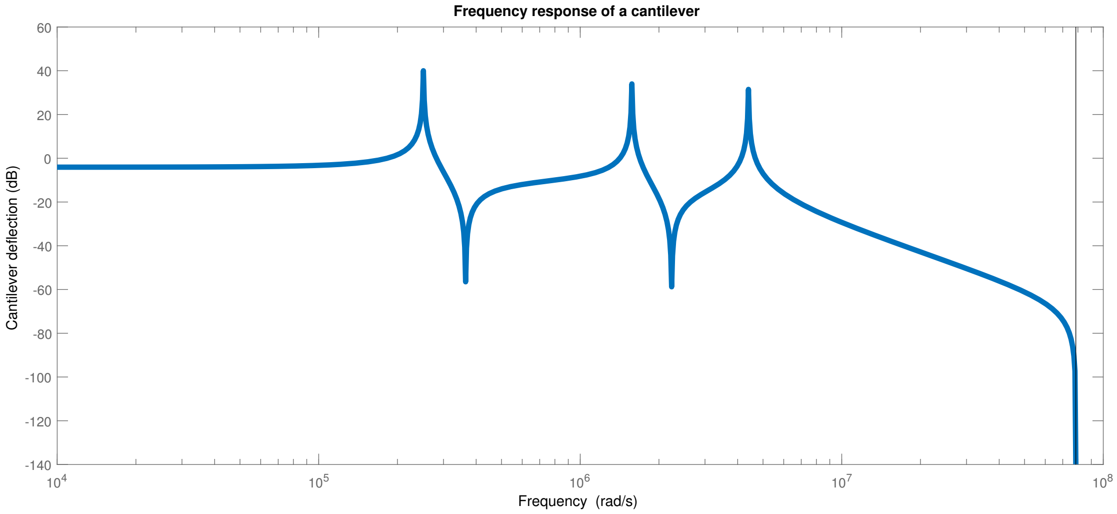

Figure 2-6: Freqeuncy response of a cantilever, depicting band pass characteristics.

By passively tuning the higher bending modes like in dynamically tuned cantilevers [9], harmonic cantilevers [30] or excitation of higher bending modes using external secondary dithering signal [7, 8], it is possible to include higher harmonics of the tip-sample forces and in the same time reduce the peak repulsive force. With the knowledge of modal spring constants, the above mentioned methods have helped in improving the estimate of tip-sample forces. Although it has not been possible to accurately estimate the harmonics other than those at the resonance frequency of the bending modes. Thus the problem of complete estimation of the tip-sample force is still open and requires a more in-depth approach that includes the dynamics of the cantilever in the determination of the forces.

2-3 Problem Statement

Many surface characteristics like the adhesion strength and stiffness and many electrical properties like surface potential [31] can be studied by accurately estimating the tip-sample interactions. Thus a complete information of the tip-sample interactions is of great significance. There have been studies in the past that have tried to estimate the tip-sample interactions by either introducing secondary exciting signals or changing the geometry of the cantilevers to excite second bending mode. In the above methods the authors assume the cantilever to obey Hooke's law and estimate the tip-sample interactions as scaled values of the cantilever deflection. This assumption fails while estimating the harmonics of tip-sample interactions. Thus, an in depth approach that includes the dynamics of the cantilever is necessary for accurate estimation of the interactions. Keyvani et. al [11] have designed a Kalman filter to estimate the tip-sample interactions as states of a linear system. In the definition of the regularized kalman filter the author assumes that the cantilever dynamics, i.e the state space matrices of the cantilever, are known before hand. In general the state space representation of the cantilever is not readily available and needs to be estimated using any of the identification techniques.

The fast growth of the field of systems and controls has witnessed the application of the theories of systems and controls, system identification in particular, to the field of atomic force microscopy. There have been lots of researches where system identification has been used to establish the dynamics of the atomic force microscope. But in all these cases the state space matrices of the raster scanner is identified in order to implement accurate feedback strategies [32, 33] and not much on the state space matrices of the cantilever. The research in this field is still in its nascent stages. This thesis project aims at applying the theories of system identification to accurately model the dynamics of the cantilever that can further be used to accurately estimate tip-sample interactions in TM-AFM.

Figure 2-7 represents the block diagram of the cantilever with the various inputs and outputs. U_d is the dithering signal whose frequency is usually near the fundamental resonance frequency of the cantilever. U_u is the interaction between the cantilever and the sample surface with which the cantilever is engaged in tapping mode. It is not possible to place any sensor to measure these interactions directly and hence these forces are unknown (marked red). Y_u is the deflection signal of the cantilever. For rectangular and harmonic cantilevers, the deflection signal will only be in the vertical direction but for torsional cantilevers, the deflection signal will include torsional deflection alongside the vertical deflections. For rectangular and harmonic cantilevers, since the probe tip is symmetrically placed, the torsional stiffness constant is orders of magnitudes higher than the flexural stiffness constants and hence the torsional deflections are negligible.

Problem Statement from System Identification Perspective

To determine the state space matrices of the cantilever in the presence of an unmeasurable input (U_u).

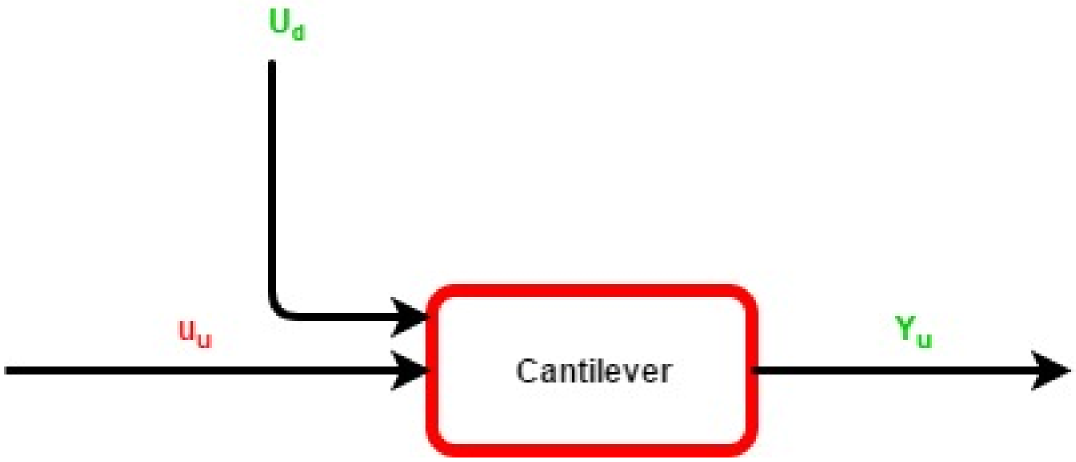

Figure 2-7: Cantilever block diagram with the different inputs and outputs.

Observing the list of signals available from experimentation, it can be immediately seen that identification of the imaging cantilever is an unknown input identification. This falls into a special group of identification techniques called blind identification [34, 35]. The success of these blind identification depend on the knowledge of the statistical properties of the input. In TM-AFM, there is no information available about the tip-sample interactions. Thus, with the incompetency of blind identification techniques, an estimate of the tip-sample interactions is obtained by using the periodic property of tip-sample interactions using the experimental set-up explained in [1]. The estimated tip-sample interactions are used to estimate a transfer function between the deflection of the cantilever and the estimated forces. The transfer between cantilever deflection and the dithering signal is found out by dithering the cantilever in free air using a suitable chirp signal.

A curve fitting technique is used to find the transfer between the tip-sample interaction and the cantilever deflection signal. The technique is based on iterative-linear least squares and S-K iterations [36] and fits a transfer function to the frequency response of the cantilever obtained at several frequencies. The proposed algorithm is tested on both simulated data as well experimental data. A detailed explanation of the proposed algorithm is dealt with in the next chapter.

Chapter 3

Frequency Domain Identification

The previous chapter dealt with the working principle of TM-AFM and its application in the industry, the problems faced by the current techniques in estimating the tip-sample forces and the necessity to include the dynamics of the cantilever in their estimation. In this chapter the identification technique adapted to arrive at the state space matrices of the cantilever is discussed in detail. The result obtained by applying the developed algorithm on simulated and experimental data are presented and discussed in the following chapter.

3-1 Experimental set-up

Figure 2-2 depicts the case in which the cantilever of an AFM is engaged with a sample surface in tapping mode. Due to the periodic motion of the cantilever in TM-AFM, the tip-sample interactions are also periodic. It is well known that a periodic signal of frequency f is composed of harmonics whose frequencies are integer multiples of the fundamental frequency. Due to the band pass filter characteristics of the cantilevers used in atomic force microscopy, the output deflection signal contains very less information about the harmonics of tip-sample interactions. This hinders the accurate estimation of the tip-sample interactions and also does not provide adequate information to identify the cantilever dynamics.

To overcome the problem stated previously , the experimental set-up as suggested in [1] is used for this thesis. The set-up, as shown in Figure 3-1, utilizes two cantilevers with different fundamental resonance frequencies. The cantilever on top is called the imaging cantilever whereas the one below is called the sensing cantilever. The sensing cantilever acquires its name from the purpose for which it is used in the set up (to sense the force exerted by the tip of the imaging cantilever). Like in the TM-AFM, the imaging cantilever is dithered at or near its resonance frequency. The sensing cantilever is chosen in such a way that its fundamental resonance frequency is at least 15 times higher than the resonance frequency of imaging cantilever. This ensures that the higher harmonics contained in the tip-sample interaction forces lie well within the static regime of the sensing cantilever. At every oscillation the imaging

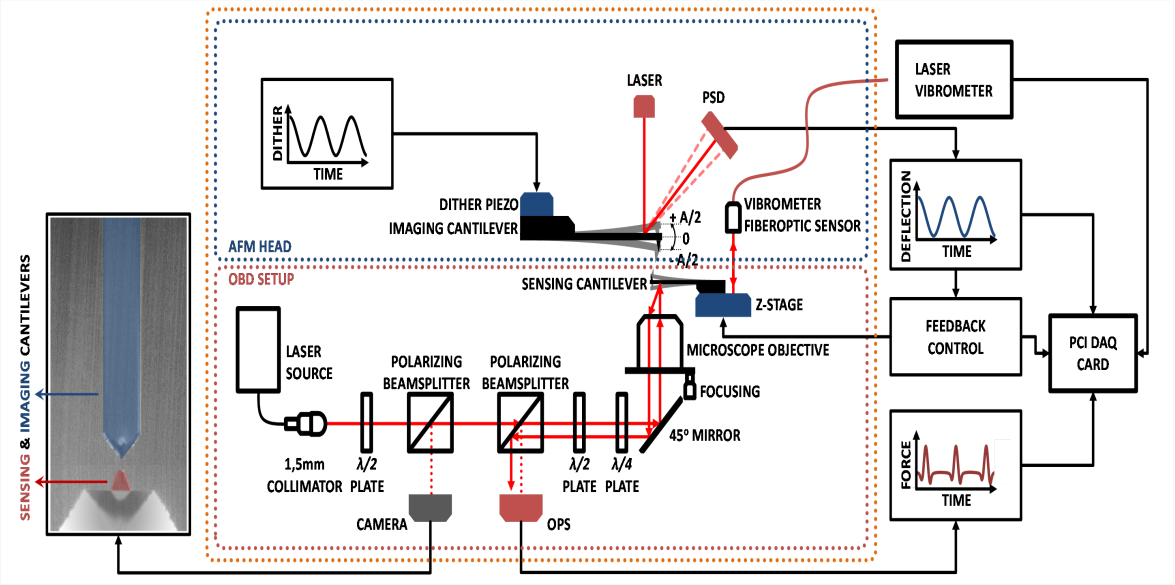

Figure 3-1: Experimental set-up as suggested in [1].

cantilever comes in contact with the sensing cantilever, thus imparting a force onto its surface which causes the deflection of the sensing cantilever. In the static regime of the sensing cantilever, the attenuation is equal to the effective spring constant of the cantilever. Thus the components of the tip-sample force with frequencies lesser than the resonance frequency of the sensing cantilever can be quantified using the spring constant of the cantilever and the deflection signal. Using Newtons 3^{rd} law of motion, which states "Every action has an equal and opposite reaction", it is acceptable to say that the force experienced by the two cantilevers are equal. The sensing cantilever is placed horizontal and the imaging cantilever placed at an angle to ensure that the only contact between the imaging cantilever and the sensing cantilever is via the tip of the imaging cantilever.

The deflections of the cantilevers are measured using the beam deflection method. $\omega_{sensing}$ and $\omega_{imaging}$ are the fundamental resonance frequencies of the sensing and imaging cantilever respectively. Theoretically it is possible to capture around $\frac{\omega_{sensing}}{\omega_{imaging}}$ harmonics of the tip-sample forces by using the above mentioned force measurement set-up thus improving the estimation of the tip-sample interactions. For accurate measurements of the deflections of the imaging and the sensing cantilevers a special calibration technique as explained in [1] is required.

3-2 Estimation of Tip-Sample Interactions

From the literature it follows that there are two ways to deal with the system with an unknown input. The first method involves the estimation of the tip-sample interactions by inverting the model of the sensing cantilever or by using the difference equation of the sensing cantilever to arrive at the tip-sample interactions. The model of the sensing cantilever (will come back to this later in the chapter) is assumed to be strictly proper, inversion of which leads to an improper and physically unrealizable transfer function. In [37] a method is proposed to tackle this issue by introducing fast poles to the inverted system to make it physically realizable. Since the poles and zeros of the cantilever are extremely large, the addition of fast poles to the inverted system might influence the true dynamics of the inverted system thus estimating the tip-sample interactions imperfectly.

The second method is to convert the unknown input problem into a state estimation problem as shown in [11] and then apply identification techniques to estimate the model of the cantilever. For the system identification procedure to yield an appropriate mathematical model, the input to the system should be sufficiently exciting. Transforming the unknown input into a state, yields a system with the dithering signal as the only input. Since the dithering signal is a single frequency signal, identification of such a system results in an unsatisfactory estimate.

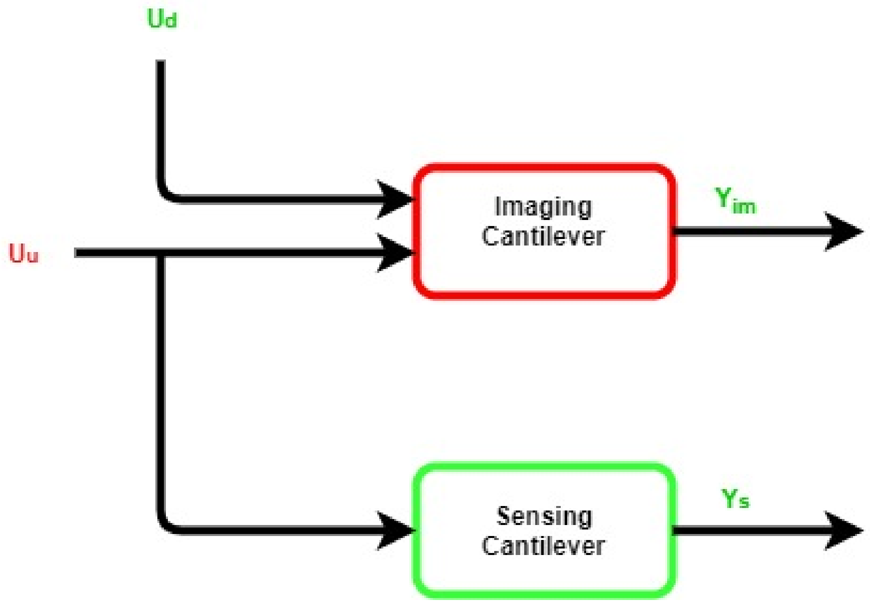

Figure 3-2: Represent of the Experimental Set-Up using blocks.

Figure 3-2 depicts the experimental set-up discussed in the previous section in the form of a block diagram. As explained before Y_{im} and Y_s represent the deflections of the imaging cantilever and the sensing cantilever respectively. Signal U_u is the unmeasurable tip-sample interactions between the imaging cantilever and the sensing cantilever and U_d is the dithering signal with a frequency around the fundamental resonance frequency of the imaging cantilever. When the imaging cantilever taps on the sensing cantilever, it exerts a force on to the sensing cantilever due to which it moves vertically. Notice that the two cantilevers will experience the same forces in terms of magnitude however the force signal on the imaging cantilever is phase shifted by π radians.

The sensing cantilever is chosen with a resonance frequency that is at least 15-20 times that of the imaging cantilever. This enables the possibility to extract information about the higher harmonics of the tip-sample interactions. Since the first few modes of the imaging cantilever lie within the static region of the sensing cantilever, it is sufficient to model the sensing cantilever using one bending mode. The dynamics of the sensing cantilever can be represented using the following equations

$$\begin{aligned} \dot{x_s} &= A_s x_s + B_s u_u + \omega_s \\ y_s &= C_s x_s + D_s u_u + v_s \end{aligned} \tag{3-1}$$

Variables x_s and y_s represent the states and deflection of the sensing cantilever respectively whereas the signal u_u represents the unmeasurable tip sample interactions between the imaging cantilever and the sensing cantilever.

The dynamics of the sensing cantilever can be represented by using a simple mass spring damper system. Assuming the mass of the sensing cantilever to be m_s, the spring constant to be k_s and the damping coefficient to be c_s, the dynamics of the sensing cantilever can be represented by a simple 2 DOF differential equation

$$m_s \ddot{z} + c_s \dot{z} + k_s z = u_u$$

Variable z in the previous equation is the deflection of the sensing cantilever and the successive derivatives are velocity and acceleration variables. Assuming the state vector $x_s = \begin{bmatrix} \dot{z} & z \end{bmatrix}^T$ the second order differential equation can be represented in the state space form as

$$\begin{aligned} \dot{x_s} &= \begin{bmatrix} \frac{-c_s}{m_s} & \frac{-k_s}{m_s} \\ 1 & 0 \end{bmatrix} x_s + \begin{bmatrix} \frac{1}{m_s} \\ 0 \end{bmatrix} u_u + w_s \\ y_s &= \begin{bmatrix} 0 & 1 \end{bmatrix} x_s + v_s \end{aligned} \tag{3-2}$$

with w_s being the process noise. The output of the state space representation y_s is the deflection signal z with an associated measurement noise v_s that is $y_s = z + v_s$. Since the tip-sample interactions affect the dynamics of the sensing cantilever and not the output directly, the feed through matrix is considered **zero**.

Since the atomic force microscopy is operated in tapping mode with a frequency at or near the fundamental frequency of the imaging cantilever, the tip-sample interactions are periodic as well with the fundamental frequency same as that of the dithering signal. Every periodic signal can be expressed as a summation of signals with frequencies that are integer multiples of the fundamental frequency and since the dithering signal is a sinusoid it is possible to decompose the tip-sample interactions into its harmonic components as

$$u_u = A_1 e^{j\omega_d} + A_2 e^{j2\omega_d} + \ldots + A_n e^{jn\omega_d}$$

with ω_d being the frequency of the dither signal, A_i being the magnitude of the i^{th} harmonic and n being the number of harmonics of the tip-sample interactions. The contributions of the harmonics to the tip sample forces reduces with higher harmonics. Thus the choice of number of harmonics to estimate the tip-sample interactions accurately is based on the **Fast Fourier Transform** (FFT) of the deflection signal of sensing cantilever.

Each of the harmonic components of the tip-sample interactions can be uniquely represented by using a complex number $u(w) = u_1 + iu_2$, the magnitude of which gives the magnitude of the harmonic component and $tan^{-1}(\frac{u_2}{u_1})$ gives the phase of the harmonic component in the signal.

The sensing cantilever represented in Equation 3-2 is in the continuous domain and can be converted into digital domain using the ZOH discretization resulting in a state space representation given as

$$\begin{aligned} x_s(k+1) &= A_{ds}x_s(k) + B_{ds}u_u(k) + w_k \\ y_s(k) &= C_{ds}x_s(k) + v_k \end{aligned}$$

with A_{ds}, B_{ds}, C_{ds} being the digital domain counterparts of the continuous time state space matrices. With such a state space representation the frequency response $H_s(\omega)$ of the sensing cantilever at a frequency ω can be calculated using the following formula

$$H_s(\omega) = C_{ds}(i\omega T_s - A_{ds})^{-1}B_{ds}$$

The frequency response at a particular frequency can also be represented as a complex variable, say $H_s(\omega) = H_1 + iH_2$. Deflection signal of the sensing cantilever is made up of the same harmonics as that present in the tip-sample forces, the reason being that the sensing cantilever is approximated as a linear system. The deflection signal of the sensing cantilever is also made up of a signal whose frequency is equal to its fundamental resonance frequency. In the sub-resonance modes, if the fundamental frequency is such that it is Q-factor times lesser than the fundamental frequency, the cantilever starts to resonate. Due to the choice of specific cantilevers for the experiment, the operational frequency is always more than the factor ($\frac{\omega_n}{Q}$, Q being the Q-factor of the cantilever) [11]. Each of the harmonic components of the sensing cantilever deflection can be represented by a complex number say $y_s(\omega) = y_1 + iy_2$. The relationship between the input and output at each of the frequencies is given by

$$(u_1 + iu_2) \times (H_1 + iH_2) = y_1 + iy_2 \tag{3-3}$$

The above equation is derived from the fact that convolution in time domain is equivalent to multiplication in frequency domain. With a measurable sensing cantilever deflection signal and knowledge about the frequency response of the sensing cantilever, the input complex number can be easily obtained by simple division. In order to prove that the above equation has a unique solution, it is represented in matrix notation by equating the real and imaginary parts

$$\begin{aligned} &(u_1 + iu_2) \times (H_1 + iH_2) = y_1 + iy_2 \\ \implies &u_1H_1 - u_2H_2 + i(u_1H_2 + u_2H_1) = y_1 + iy_2 \\ \implies &\begin{bmatrix} H_1 & -H_2 \\ H_2 & H_1 \end{bmatrix} \begin{bmatrix} u_1 \\ u_2 \end{bmatrix} = \begin{bmatrix} y_1 \\ y_2 \end{bmatrix} \\ \implies &\begin{bmatrix} u_1 \\ u_2 \end{bmatrix} = \begin{bmatrix} H_1 & -H_2 \\ H_2 & H_1 \end{bmatrix}^{-1} \begin{bmatrix} y_1 \\ y_2 \end{bmatrix} \\ \implies &u = H^{-1}y \end{aligned}$$

The matrix H^{-1} in the above equation is a full rank matrix in the bandwidth of interest thus establishing the fact that complex number $u(\omega)$ thus determined is unique. This algorithm will face a problem when the magnitude of the sensing cantilever is very small in which case the H^{-1} matrix gets close to being singular, which usually occurs at very high frequencies. Although at such high frequencies the contributions of the tip-sample interactions are insignificant.

The number of harmonics of the tip-sample interactions is determined from the FFT of the deflection of the Sensing cantilever. The complex number $y_s(\omega)$ in the above equation can be determined using Discrete Fourier Transform (DFT) of the sensing cantilever deflection signal which is given as

$$y_s(\omega_j) = \sum_{n=0}^{N-1} y_s(n).e^{-i\omega_j}$$

where $y_s(n)$ represents the n^{th} sample of the deflection signal. By identifying the complex number associated with each of the frequency components, the tip-sample interactions can be reconstructed as

$$u = \sum_{j=1}^{n_u} |u(\omega_j)| sin(\omega_j t + \angle u(\omega_j))$$

where ω_j is the complex number associated with the j^{th} harmonic with a magnitude of $|u(\omega_j)|$ and an associated angle $\angle u(\omega_j)$.

3-3 Signal Averaging and Noise Floor

Any practical measurement is always subjected to noise or unwanted signals. The study of these signals is necessary to determine if it is possible to separate a physical signal from noise at particular frequencies. The main source of noise in AFM is from the deflection sensing set up. Noises include the thermal noise of the cantilever, shot noise present in the photo-diode, fluctuations in laser intensity and Johnson noise due to heating of resistors and capacitors present within the electronics. Tamer et. al in [1] studies the measurement noise of the OBD set up. The author uses the same set up as used for this thesis. The author measures the noise spectrum of the OBD set up with the use of a data acquisition (DAQ) card when the cantilevers are not engaged in tapping mode. The author measures the noise floor of the deflection measurement set to be $400fm/\sqrt[2]{Hz}$. This experimentally obtained noise floor is lesser than the thermal noise of the cantilever. Since the set up used is the same except for the cantilevers, the same noise floor can be considered for this thesis.

Also, the signals are averaged before they are further used for imaging cantilever estimation. Averaging a signal has been a very successful technique in the field of signal processing to increase the strength of the signal with respect to noise affecting it. By averaging a signal N times, the signal-noise ratio (SNR) is increased by a factor of N. The mathematical proof for the same can be found in the **APPENDIX**. The performance of the developed identification algorithm in the presence of noise is studied in the next chapter.

3-4 Transfer Function Estimation for the Imaging cantilever

Having estimated the unmeasurable tip-sample interactions, the unknown input system identification problem is now converted into known inputs estimation problem with some uncertainties in the input. For the system identification to yield fruitful results it must be ensured that the input is persistently exciting. In general the persistence of excitation of the input signal is based on a certain covariance function, but in simpler terms an input can be called persistently exciting if it has good frequency content within the bandwidth of interest. In order to ensure persistency of excitation, the tapping experiments are performed at three different frequencies near the fundamental resonance frequency of the imaging cantilever. The first two data-sets are obtained by tapping at a frequency where the free air amplitude is 5% lesser than the maximum amplitude of oscillation, on either sides of the fundamental resonance frequency and the third data-set is obtained at a random frequency above the fundamental frequency. This experimentation method ensures that there are enough frequency points to accurately identify imaging cantilever.

Assuming the frequency response of the imaging cantilever to be H_{im}, the response at a specific frequency $H_{im}(\omega)$ can be represented as a complex number say $H_{im1} + iH_{im2}$. With the knowledge of deflection signal of the imaging cantilever and the estimated tip-sample interactions, the respective complex numbers, $y_{im1} + iy_{im2}$ and $u_1 + iu_2$ can be obtained as explained earlier. The relationship between the complex numbers at each frequency can be represented as

$$(u_1 + iu_2) \times (H_{im1} + iH_{im2}) = y_{im1} + iy_{im2} \tag{3-4}$$

Thus the response of the system at a specific frequency can be obtained from Equation 3-4. To prove the uniqueness of the frequency response value, equation 3-4 is represented in matrix form as shown

$$\begin{bmatrix} u_1 & -u_2 \\ u_2 & u_1 \end{bmatrix} \begin{bmatrix} H_{im1} \\ H_{im2} \end{bmatrix} = \begin{bmatrix} y_{im1} \\ y_{im2} \end{bmatrix}$$

$$\implies \begin{bmatrix} H_{im1} \\ H_{im2} \end{bmatrix} = \begin{bmatrix} u_1 & -u_2 \\ u_2 & u_1 \end{bmatrix}^{-1} \begin{bmatrix} y_{im1} \\ y_{im2} \end{bmatrix}$$

Since the complex numbers at every frequency component is uniquely determined and since only the harmonics that contribute significantly to the tip-sample interactions are considered, the square matrix in the above equation is full rank. Thus the frequency response of the imaging cantilever is uniquely determined.

With the knowledge about the response of the system at several frequencies, the transfer function needs to be estimated. There have been several methods in literature that try to estimate a system using frequency response data. One of the earliest approaches dates back to 1959 where Levy [38] tries to fit the frequency response data using a transfer function. The author tries to estimate the transfer function coefficients by minimizing the error between an ideal transfer function model that represents the data accurately and an approximate transfer function model that fits the points as good as possible. The author assumes that the ideal transfer function is available but in general case it is not possible to obtain such an ideal transfer function model.

Subsequent works in the field of transfer function estimation try to minimize the sum of square of errors ($\epsilon(\omega_k)$) between the output and the estimated output at various frequency points.

$$\begin{aligned}\epsilon(\omega_k) &= y(\omega_k) - \sum_{i=1}^{n_u} \frac{N_i(\omega_k)}{D(\omega_k)} u_i(\omega_k)\\ \epsilon(\omega_k)D(\omega_k) &= y(\omega_k)D(\omega_k) - \sum_{i=1}^{n_u} N_i(\omega_k)u(\omega_k\\ &= \epsilon^{'}(\omega_k)\end{aligned} \tag{3-5}$$

The minimization problem of the sum of squares of the error can be written as

$$\begin{aligned}&\underset{D,N_i}{\text{minimize}} \sum_{k=1}^{n_w} W(\omega_k)\left(y(\omega_k) - \sum_{i=1}^{n_u} \frac{N_i(\omega_k)}{D(\omega_k)} u_i(\omega_k)\right)^2\\ &\underset{D,N_i}{\text{minimize}} \sum_{k=1}^{n_w} \frac{W(\omega_k)}{D(\omega_k)}\left(y(\omega_k)D(\omega_k) - \sum_{i=1}^{n_u} N_i(\omega_k)u(\omega_k)\right)^2\end{aligned} \tag{3-6}$$

It can be noticed from the structure of the optimization problem that the term within the brackets is a simple least squares problem. The modified weighting matrix $\frac{W(\omega_k)}{D(\omega_k)}$ complicates the optimization problem. Thus the earliest methods try to estimate the transfer function by minimzing the modified error $\epsilon^{'}(\omega_k)$ rather than minimizing the actual error. The problem formulation in the previous equation has a major drawback associated with it. If the system has poles such that the denominator polynomial varies over a large range through the experimental points, then large errors would be introduced thus yielding erroneous results.

Sanathanan et. al [36] proposed a way to solve the above non linear problem into a series of linear least squares problem by reformulating the optimization procedure. The following cost function is minimized rather than the cost function as shown in Equation 3-6

$$\underset{D_m,N_{i,m}}{\text{minimize}} \sum_{k=1}^{n_w} \frac{W(\omega_k)}{D_{m-1}(\omega_k)}\left(y(\omega_k)D_m(\omega_k) - \sum_{i=1}^{n_u} N_{i,m}(\omega_k)u(\omega_k)\right)^2 \tag{3-7}$$

For the frequency domain identification (frequency response data), the minimization problem in the previous step can be rewritten as

$$\underset{D_m,N_{i,m}}{\text{minimize}} \sum_{k=1}^{n_w} \frac{W(\omega_k)}{D_{m-1}(\omega_k)}\left(H_{im}(\omega_k)D_m(\omega_k) - \sum_{i=1}^{n_u} N_{i,m}(\omega_k)\right)^2$$

In the above equation, $N_{i,m}, D_m$ are the numerator and the denominator polynomials that are estimated in the m^{th} iteration whereas D_{m-1} is the denominator polynomial estimated in the $m-1^{th}$ iteration. The iterations are initialized with $D_0 = 1$. The above reformulation converts the nonlinear problem to an iterative least squares problem which can be solved using the optimization techniques already available. The iterations are popularly known as S-K iterations arising from initials of the researchers who introduced this technique.

Assuming $D = \sum_{j=1}^{r} b_j z^j$ and $N = \sum_{j=0}^{r-1} a_j z^j$, the above given least square problem can be re written as

$$\underset{a_i,b_i}{minimize} ||\Delta_k(\beta_{k+1}s^{k+1} - h)||^2 \tag{3-8}$$

where the variables β and Δ are defined as

$$\beta_k = \begin{bmatrix} 1 & \omega_1 & \omega_1^2 & \cdots & \omega_1^{r-1} - H_{im}(\omega_1)\omega_1 & \cdots & -H_{im}(\omega_1)\omega_1^r & \\ 1 & \omega_2 & \omega_2^2 & \cdots & \omega_2^{r-1} - H_{im}(\omega_2)\omega_2 & \cdots & -H_{im}(\omega_2)\omega_2^r & \\ \vdots & \vdots & \vdots & \vdots & \vdots & \vdots & \vdots & \vdots \\ 1 & \omega_{n_f} & \omega_{n_f}^2 & \cdots & \omega_{n_f}^{r-1} - H_{im}(\omega_{n_f})\omega_{n_f} & \cdots & -H_{im}(\omega_{n_f})\omega_{n_f}^r & \end{bmatrix}$$

$$h = \begin{bmatrix} H_{im}(\omega_1) \\ H_{im}(\omega_2) \\ \vdots \\ H_{im}(\omega_{n_f}) \end{bmatrix}$$

$$\Delta_k = diag\left(\frac{W(\omega_i)}{D_{k-1}(\omega_i)} \right)$$

The update s^{k+1} is the least squares solution of the minimization problem discussed above. This solution yields sequence of polynomial coefficients for both numerator and denominator. Thus the algorithm start off with $D_0 = 1$ and iteratively estimates the numerator and the denominator polynomials. For the successive iterations the the numerator and denominator polynomials are expressed in terms of orthogonal rational basis function given by

$$R_{j,m}(\omega) = (\frac{\sqrt[2]{1 - |\lambda_{j,m-1}|^2}}{q(\omega) - \lambda_{j,m-1}}) \prod_{r=0}^{j-1} \frac{1 - (\lambda_{j,m-1})^* q(\omega)}{q(\omega) - \lambda_{r,m-1}}$$

In this representation $\lambda_{j,m-1}$ is the j^{th} pole identified in $m - 1^{th}$ iteration, $\lambda^*_{j,m-1}$ is the complex conjugate of the and $q(\omega)$ is a frequency domain variable on the unit disk for this rational basis function. Thus the optimization procedure converges to the true poles of the system.

S-K iteration, even though it converges, does not always yield a locally optimum solution and hence further refinements of the polynomial coefficient is required. The critical points that may yield a global optimum are found using second set of iterations. The algorithm searches for a critical point by constructing a linear approximation for the non-linear equation as in 3-7. The linear equation thus obtained is solved in a linear least square sense. Equation for the j^{th} denominator parameter is given by

$$0 = 2 \sum_{k=1}^{n_f} Re \left\{ \frac{|W(\omega_k)|^2 R_j^*(\omega_k) \sum_{i=1}^{n_k} N^*_{i,m-1}(\omega_k) u_i^*(\omega_k)}{D^*_{m-1}(\omega_k) |D_{m-1}(\omega_k)|^2} \left(D_m(\omega_k) y(\omega_k) - \sum_{i=1}^{n_u} N_{i,m}(\omega_k) u(\omega_k) \right) \right\}$$

Similarly the linear equation for j^{th} numerator parameter is given as

$$0 = -2 \sum_{k=1}^{n_f} Re \left\{ \frac{|W(\omega_k)|^2 R_j^*(\omega_k) u_i^*(\omega_k)}{|D_{m-1}(\omega_k)|^2} \left(D_m(\omega_k) y(\omega_k) - \sum_{i=1}^{n_u} N_{i,m}(\omega_k) u(\omega_k) \right) \right\}$$

The linear equation for each parameter is obtained by differentiating the non-linear equation with respect to the parameter being considered. Linear refinements are initiated by using the best solution found in the S-K iterations step. The basis function corresponding to the step that yields the best solution is used and unlike in S-K iterations, the basis function remains constant.

In this chapter a detailed procedure for identification of the imaging cantilever is explained. The steps followed to arrive at an optimal result can be summarized as follows

- Obtain the modal parameters of the Sensing cantilever using the calibration procedure (explained in next chapter).
- Obtain a linear model for the Sensing cantilever using the obtained modal parameters.
- Study the FFT of the deflection of sensing cantilever to determine the harmonics of the tip-sample interactions.
- Estimate the individual complex number of the tip-sample interactions associated with each frequency and reconstruct the tip-sample interaction signal.
- Using the response of the cantilever in free air and in tapping-mode estimate the frequency response values at all the frequencies.
- Choose proper weighting vector depending on the frequency response values.
- Estimate the transfer function of the imaging cantilever using the algorithm discussed above.

Chapter 4

Simulation and Experimental Results

The previous chapter dealt with the methodology followed to arrive at the state space matrices of the imaging cantilever. A detailed explanation of the methodology involved with the unknown input estimation and system identification of imaging cantilever was stated. This chapter deals with the application of the designed algorithm on simulated as well as real time data and discusses the results thus obtained.

4-1 Results from Simulation

Before application of any algorithm on real time data it is always important to test the efficiency and performance of the algorithm with simulated data. The deflection, dithering and tip-sample interaction signals were simulated and it was ensured that these signals closely resembled the signals obtained from the dual cantilever experimental set up. The imaging cantilever was modeled as a 6^{th} order linear system that represented the dynamics of the first three bending modes of the cantilever, each mode being represented as a separate mass spring damper system. As argued earlier, the dynamics of the sensing cantilever is modeled using one mass spring damper system (one bending mode) due to its large fundamental frequency.

The model of the imaging cantilever is given by

$$\begin{aligned}
\dot{x}_{im} &= \begin{bmatrix} \frac{-c^1_{im}}{m^1_{im}} & \frac{-k^1_{im}}{m^1_{im}} & 0 & 0 & 0 & 0 \\ 1 & 0 & 0 & 0 & 0 & 0 \\ 0 & 0 & \frac{-c^2_{im}}{m^2_{im}} & \frac{-k^2_{im}}{m^2_{im}} & 0 & 0 \\ 0 & 0 & 1 & 0 & 0 & 0 \\ 0 & 0 & 0 & 0 & \frac{-c^3_{im}}{m^3_{im}} & \frac{-k^3_{im}}{m^3_{im}} \\ 0 & 0 & 0 & 0 & 1 & 0 \end{bmatrix} x_{im} + \begin{bmatrix} \frac{1}{m^1_{im}} & \frac{1}{m^1_{im}} \\ 0 & 0 \\ \frac{1}{m^2_{im}} & \frac{1}{m^2_{im}} \\ 0 & 0 \\ \frac{1}{m^3_{im}} & \frac{1}{m^3_{im}} \end{bmatrix} \begin{bmatrix} U_d \\ U_{ts} \end{bmatrix} + w_{im} \\
y_{im} &= \begin{bmatrix} 0 & 1 & 0 & 1 & 0 & 1 \end{bmatrix} x_{im} + v_{im}
\end{aligned} \tag{4-1}$$

where $k^i_{im}, c^i_{im}, m^i_{im}$ are the individual modal spring constants, modal damping coefficients and modal mass respectively. The state space system in Equation 4-1 is obtained by modeling each of the bending modes as a separate mass spring damper system with their dynamics represented by using the following differential equation

$$m^i_{im}\ddot{x}^i_{im} + c^i_{im}\dot{x}_{im^i} + k^i_{im}x^i_{im} = U_u + U_{ts}$$

Variable x^i_{im} in the equation represents the deflection of the i^{th} bending mode. The fundamental resonance frequency (f_0) of the imaging cantilever is chosen to be $40kHz$ and the higher bending modes are fixed at $6.27f_0$ and $17.54f_0$. These numbers are based upon the Euler Bernoulli equation for rectangular cantilever beams. The Q-factor of each of the modes are chosen to be 300 and the modal spring constants are fixed at 3,6,8 for the first, second and the third bending modes respectively. The increasing values of the modal spring constants indicate that the higher bending modes are stiffer than the lower modes. Using these parameters, the modal masses and the modal damping constants are calculated using the following formulas

$$\begin{aligned} m^i_{im} &= \frac{k^i_{im}}{{\omega^i_n}^2} \\ c^i_{im} &= \frac{\sqrt[2]{m^i_{im}k^i_{im}}}{Q^i_{im}} \end{aligned}$$

where ω^i_n is the resonance frequency of the i^{th} bending mode and Q^i_{im} is its respective Q-factor.

In a similar way, the dynamics of the sensing cantilever is modeled as a single mass damper system. This representation is sufficient to model its dynamics because of it large static regime. The state space representation of the sensing cantilever is given by

$$\begin{aligned} \dot{x_s} &= \begin{bmatrix} \frac{-c_s}{m_s} & \frac{-k_s}{m_s} \\ 1 & 0 \end{bmatrix} x_s + \begin{bmatrix} \frac{1}{m_s} \\ 0 \end{bmatrix} U_{ts} + w_s \\ y_s &= \begin{bmatrix} 1 & 0 \end{bmatrix} x_s + v_s \end{aligned} \tag{4-2}$$

The parameters of the cantilever are obtained from the knowledge of the resonance frequency ($\omega_s = 1.79MHz$), spring constant ($k_s = 13.5$) and Q-factor(225) of the sensing cantilever. In general the spring constant of the first mode of the cantilever can be found from the thermal fluctuations of the cantilever [39]. For simulated data it is assumed that the spring constants are known before hand but for experimental data, the spring constants of the imaging and the sensing cantilever are calibrated. The calibration technique will be explained in detail in the next section of the chapter.

Having modeled the cantilevers as mass-spring-damper systems, the tip sample interactions were simulated as a sum of sinusoids.

$$U_{ts} = \sum_{k=1}^{na} \frac{1}{k} sin(\omega_k t + rand \times \frac{\pi}{2})$$

Variable *rand* in the previous equation is a random number generated in the set [0,1]. The decreasing contributions of the higher modes are simulated using the factor $\frac{1}{k}$.

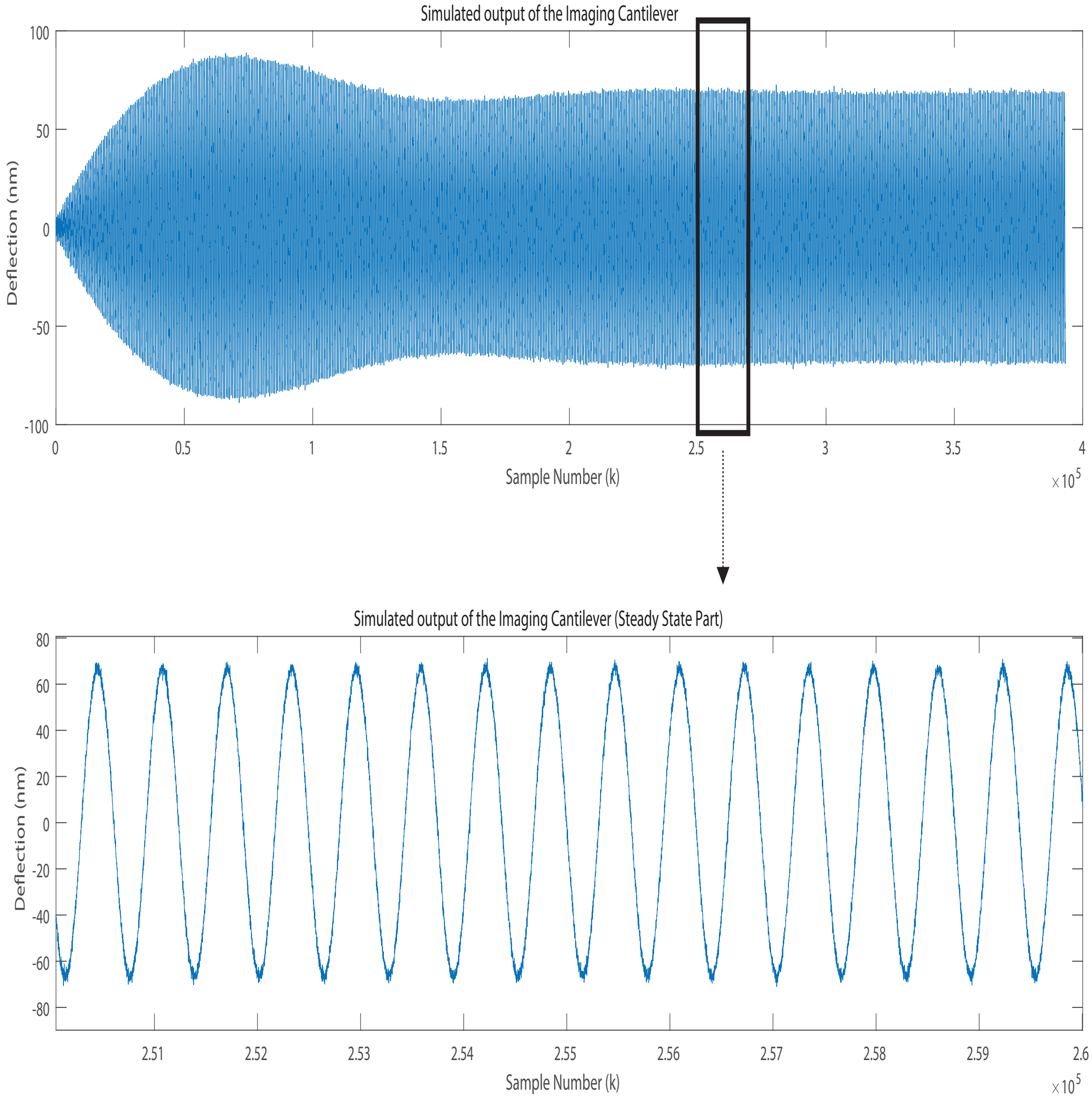

Figure 4-1: (Top) Simulated deflection of imaging cantilever. (Bottom) Steady state part of the imaging cantilever deflection.

Figure 4-1 represents the simulated deflection of the imaging cantilever. The AFM is designed to read the steady state part of the deflection signals. For this purpose the transient part of the simulated signals are removed and only the steady state response is further used for identification.

Similarly other signals are also trimmed to match with their respective input/ output pairs. White noise is added to the simulated signals to make the signals as close to the real system as possible. Tapping mode AFM is accurately simulated using the signals and the simulations are performed at three different frequencies around the resonance frequency.

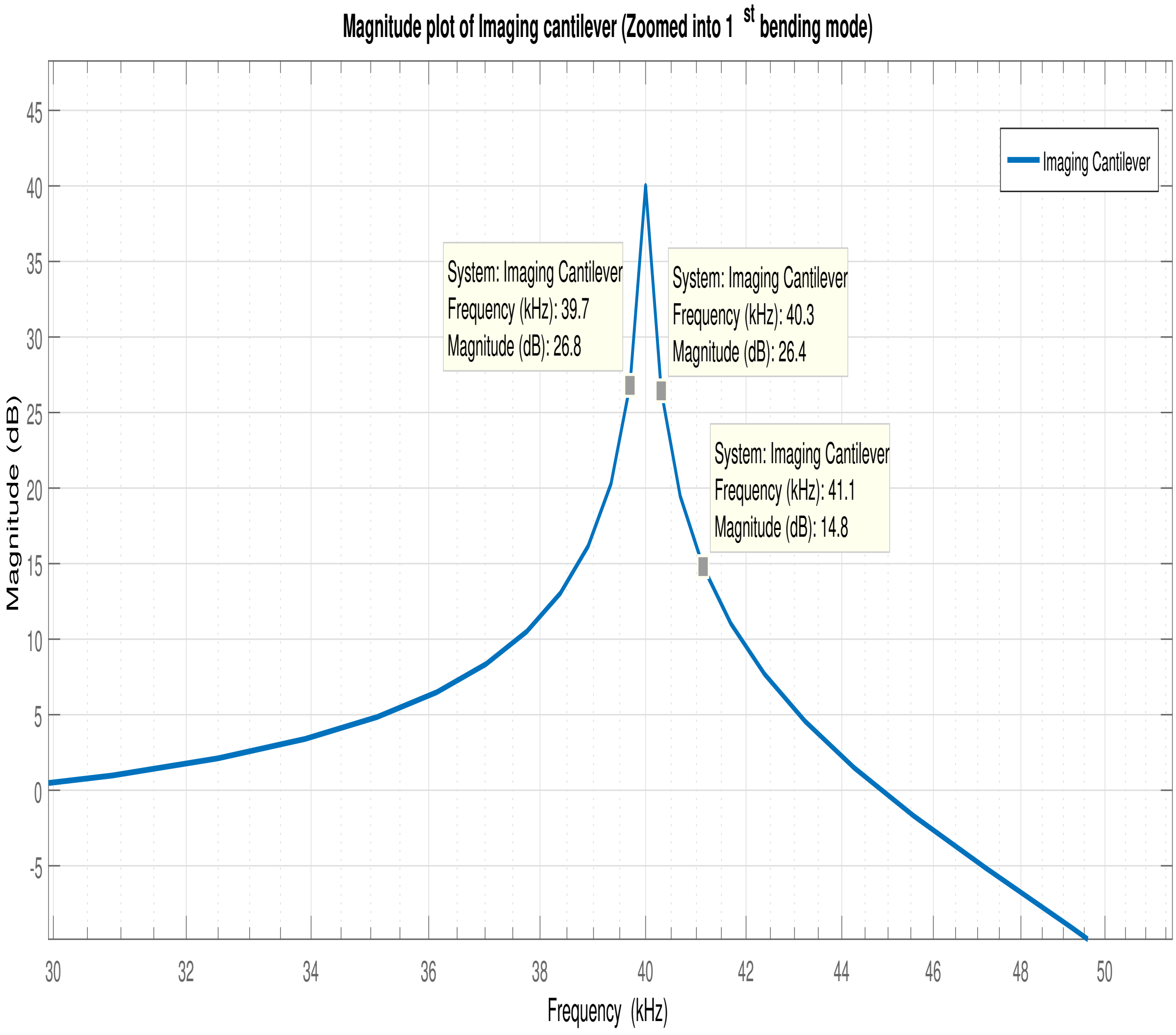

Figure 4-2: Magnitude plot of the imaging cantilever (Zoomed into first bending mode).

Figure 4-2 represents the magnitude plot of the imaging cantilever zoomed in to the fundamental resonance frequency. The data tips in the figure represents the frequencies at which the imaging cantilever is tapped on the surface of the sensing cantilever. The three points represent the frequencies where the amplitude is 5% below the maximum amplitude, 5% above the maximum amplitude and another frequency above the fundamental frequency respectively.

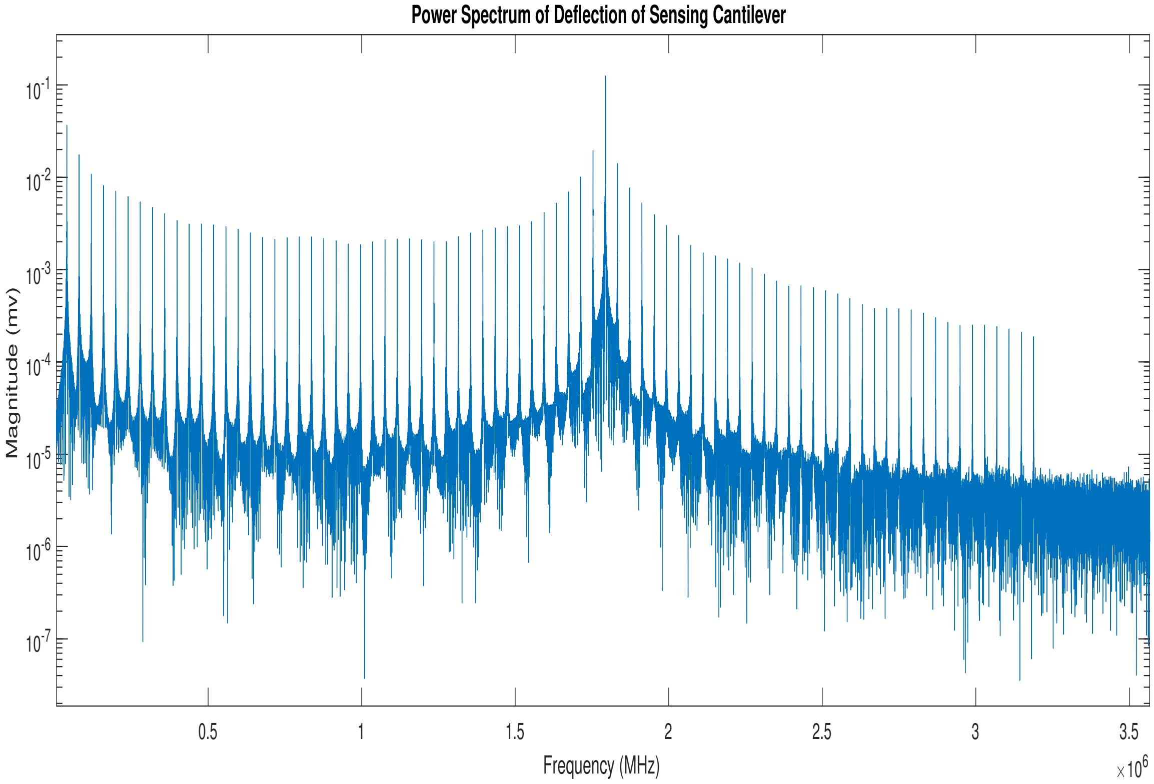

Figure 4-3: FFT of Deflection of Sensing Cantilever ($F_{tapping} = 39850Hz$).

Figure 4-3 and 4-4 represent the FFT of deflection of Sensing cantilever and the assumed tip-sample interactions respectively. It is seen from the figure that the contributions of harmonics of the tip-sample interactions over 2.5MHz to the deflection of the sensing cantilever is insignificant. Hence the tip-sample interactions can be approximated using lesser number of harmonics than present in the assumed tip-sample interactions. Looking at the FFT plot, it is concluded that the tip-sample interactions will be estimated using 60 harmonics instead of 80 harmonics present in the actual tip-sample interactions. Tapping at the other two frequencies produces similar results and hence the tip-sample interactions in each of these cases are approximated using 60 harmonics. Figure 4-5 clearly depicts the closeness of the estimated tip-simple interactions to the assumed tip-sample interactions. The algorithm for finding the harmonics of the tip-sample interactions involves inverting a certain frequency response matrix ($H(\omega)$), which tends to singularity with higher harmonics. This is attributed to the large roll-off of the sensing cantilever at very high frequencies. Thus approximating the actual-tip sample interactions accurately with lower harmonics prevents the problem of non-invertibility.

Having estimated the tip-sample interactions, the next step is to estimate the frequency response of the imaging cantilever using a similar algorithm used to determine the complex number associated with each harmonic of the tip-sample interactions. This time there is a small change in the construction of the matrices. The following equations are used to determine the frequency response of the imaging cantilever

$$u(\omega_k) \times H_{im}(\omega_k) = y_{im}(\omega_k) \tag{4-3}$$

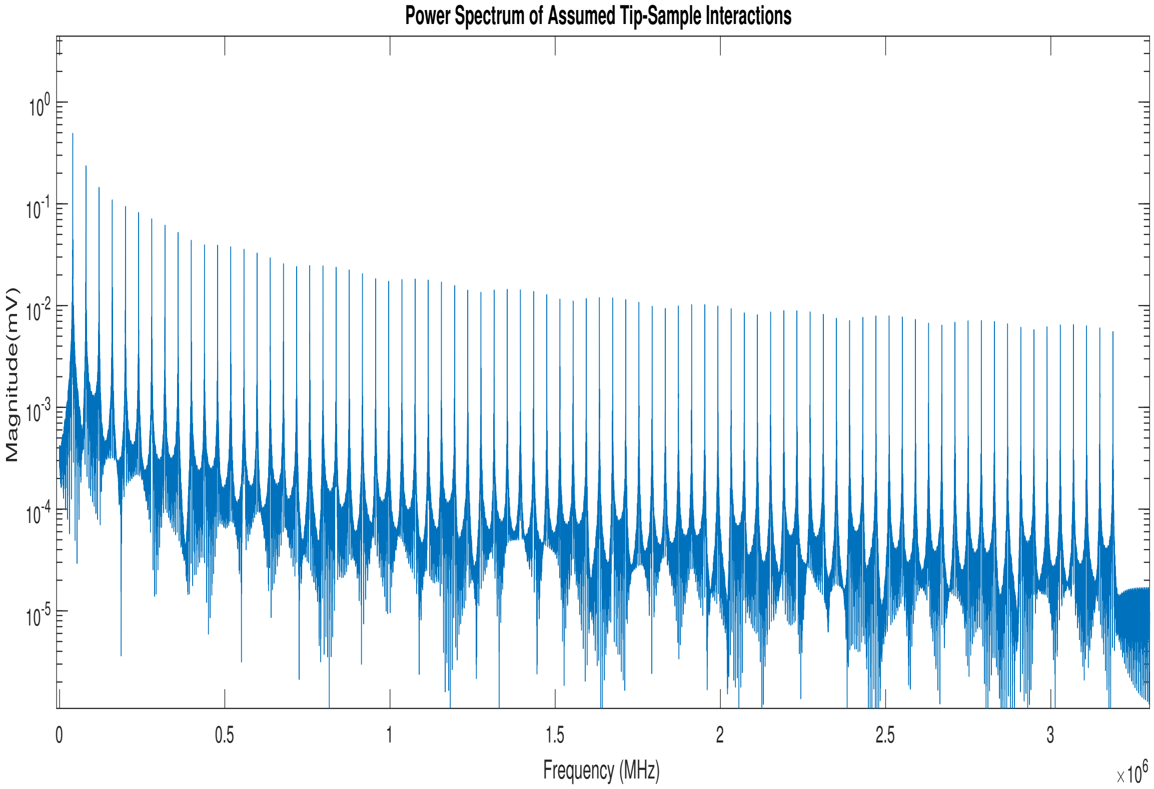

Figure 4-4: FFT of Assumed Tip-sample interactions ($F_{tapping} = 39850 Hz$).

where y_{im} is the deflection of the imaging cantilever, u is the estimated tip-sample interactions and H_{im} in this case in the transfer between imaging cantilever deflection and the tip-sample interactions. It is not possible to estimate the transfer between deflection of imaging cantilever and the dithering signal because the dithering signal does not contain any information at frequencies other than the frequency of tapping. The estimation of transfer between Imaging cantilever and the dithering signal will be dealt with later in the chapter.

Equation 4-3 can be represented in matrix notation as follows

$$(u_1 + iu_2) \times (H_1 + iH_2) = y_1 + iy_2$$
$$\implies \begin{bmatrix} u_1 & -u_2 \\ u_2 & u_1 \end{bmatrix} \begin{bmatrix} H_1 \\ H_2 \end{bmatrix} = \begin{bmatrix} y_1 \\ y_2 \end{bmatrix}$$
$$\implies \begin{bmatrix} H_1 \\ H_2 \end{bmatrix} = \begin{bmatrix} u_1 & -u_2 \\ u_2 & u_1 \end{bmatrix}^{-1} \begin{bmatrix} y_1 \\ y_2 \end{bmatrix}$$

As explained earlier the square matrix in the above equation is full rank and hence H_1 and H_2 are uniquely determined. Having determined the frequency response at different frequencies, the transfer function between the deflection of imaging cantilever and the tip-sample interactions are estimated using the algorithm explained in the previous chapter. Since the frequency vector starts close to the resonance frequency, there is no information about the behavior of the system at lower frequencies, thus resulting in improper estimation of the

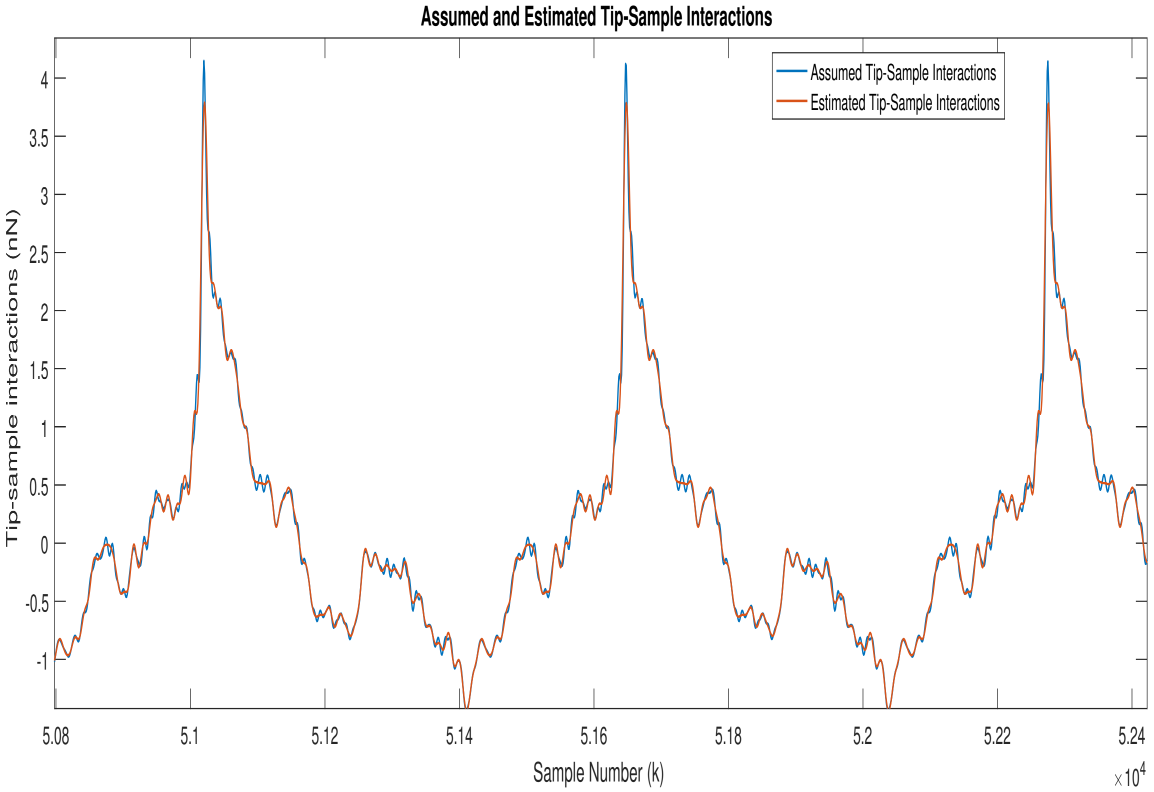

Figure 4-5: Assumed and Estimated Tip-sample interactions $(F_{tapping} = 39850Hz)$.

steady state. To improve the estimate of steady state, an extra frequency response is added to the calculated frequency response. Each mode of the imaging cantilever is assumed to be a mass spring damper system whose transfer function is given by

$$\frac{y(s)}{u(s)} = \frac{1}{k_i} \frac{(\omega_n^i)^2}{s^2 + 2\zeta(\omega_n^i) + (\omega_n^i)^2}$$

The steady state response of each of these modes is given as the reciprocal of the modal spring constants. Hence the combined steady state response of the imaging cantilever is the sum of the reciprocals of the modal spring constants.

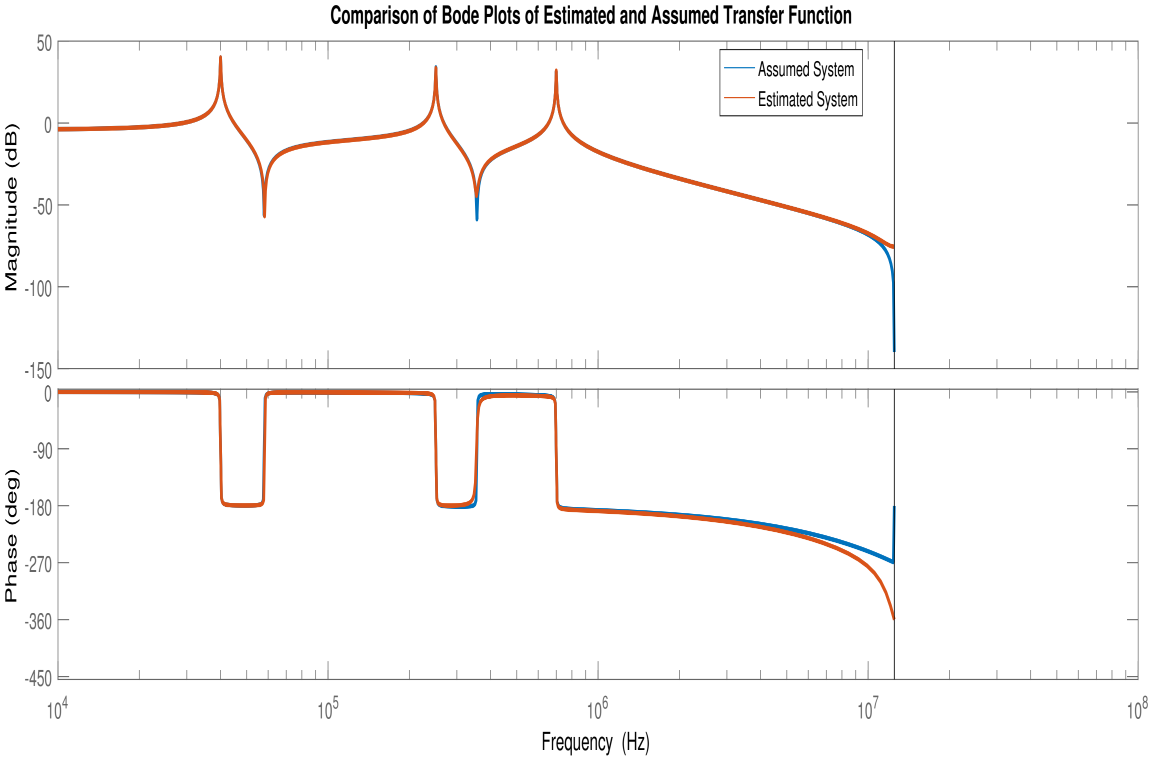

Figure 4-6: Comparison of bode plots of the Assumed(Blue) and Estimated Transfer Function(Red).

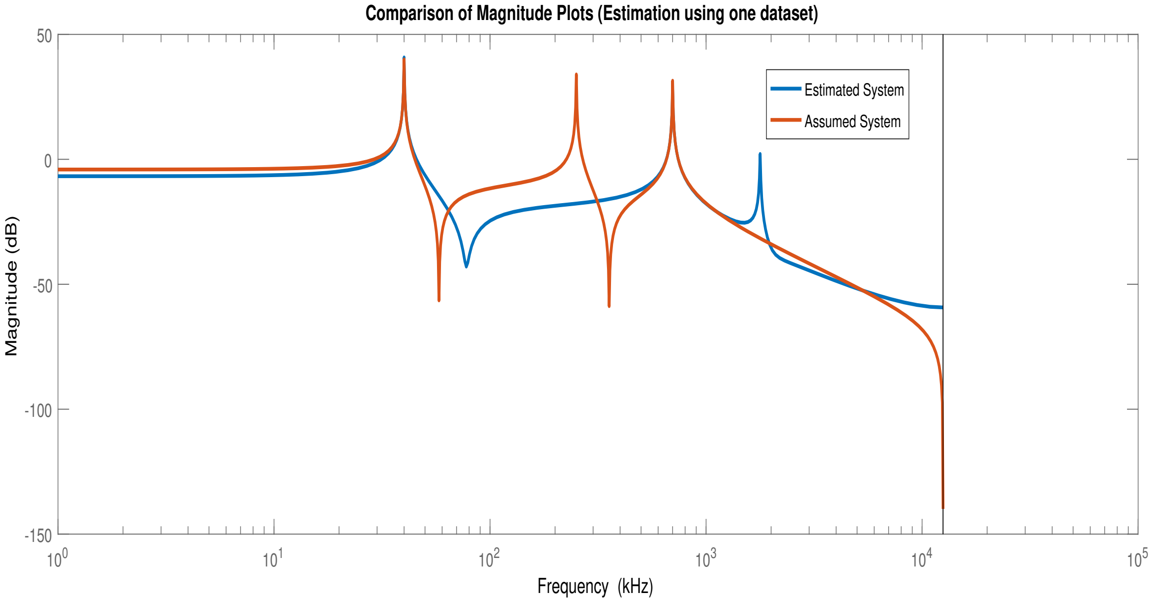

Figure 4-7: Comparison of bode plots of the Estimated(Blue) and Assumed Transfer Function(Red)[Estimated with one Data].

Figure 4-6 compares the bode plots between the estimated and the simulated data. The system is estimated using the data obtained by tapping at three different frequencies. It is seen that there is a very good fit between the estimated and the simulated transfer function. A clear difference is evident in Figure 4-7 which is obtained by estimating with only one data set. Clearly the estimation of the system is not accurate thus proving the importance to combine the experiments for the estimation process.

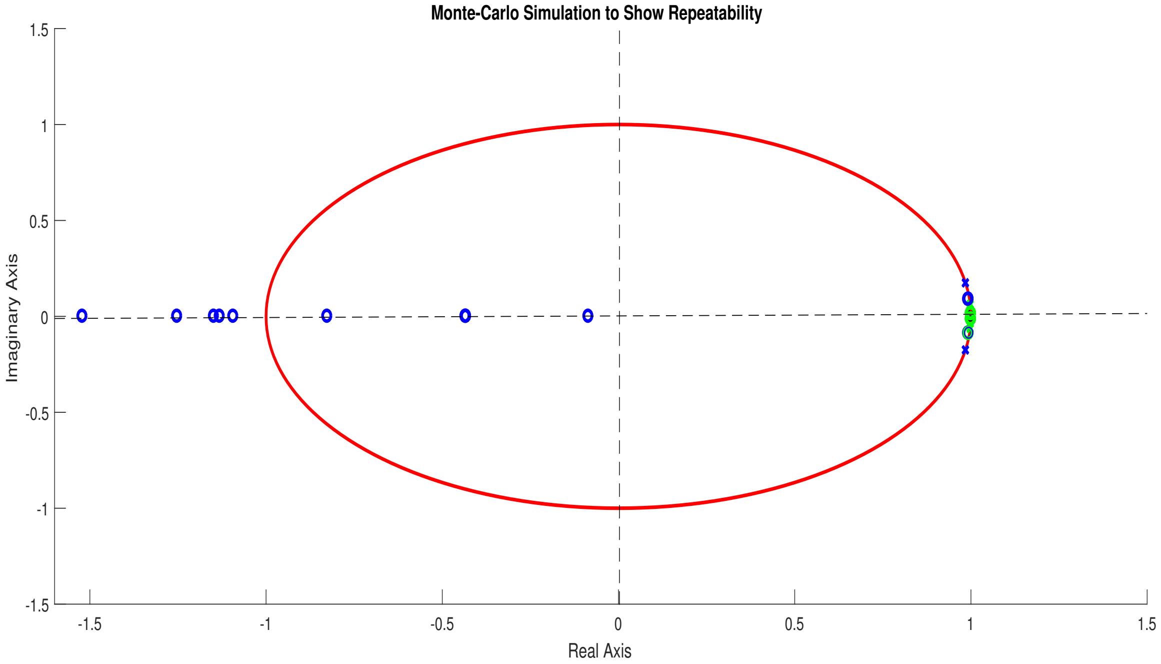

Figure 4-8: Plot of poles and zeros of the estimated system for 10 iterations.

Figure 4-8 shows the pole zero plot of the the estimated system for 10 iterations. From the figure it appears as if the successive iterations estimate the complex poles and zeros at the same value. The zeros on the negative side of the unit circle represents the zero induced due to discretization of the continuous system. Since these zeros are introduced at very high frequencies, the dynamics of the cantilever is not affected by them. Figure 4-9 represents the zoomed pole zero plot seen previously, zooming into one of the poles. It is seen clearly that there is not much of difference between the successive estimation of the pole for ten iterations. The difference arises only in the 5^{th} decimal place thus establishing the repeat-ability of the estimation process.

Figure 4-10 compares the bode plot of the estimated system at different noise levels with the actual system. It is seen that the higher noise levels do not affect the accurate estimation of poles of the system, but only affect the estimation of the zeros. Still there is not much of difference between the estimated zeros. Moreover the accepted levels of noise in the industry for Atomic Force Microscopy is at most $30dB$ and the proposed algorithm seems to work well within this noise level.

The estimation method fails to accurately identify the system at high noise level. Figure

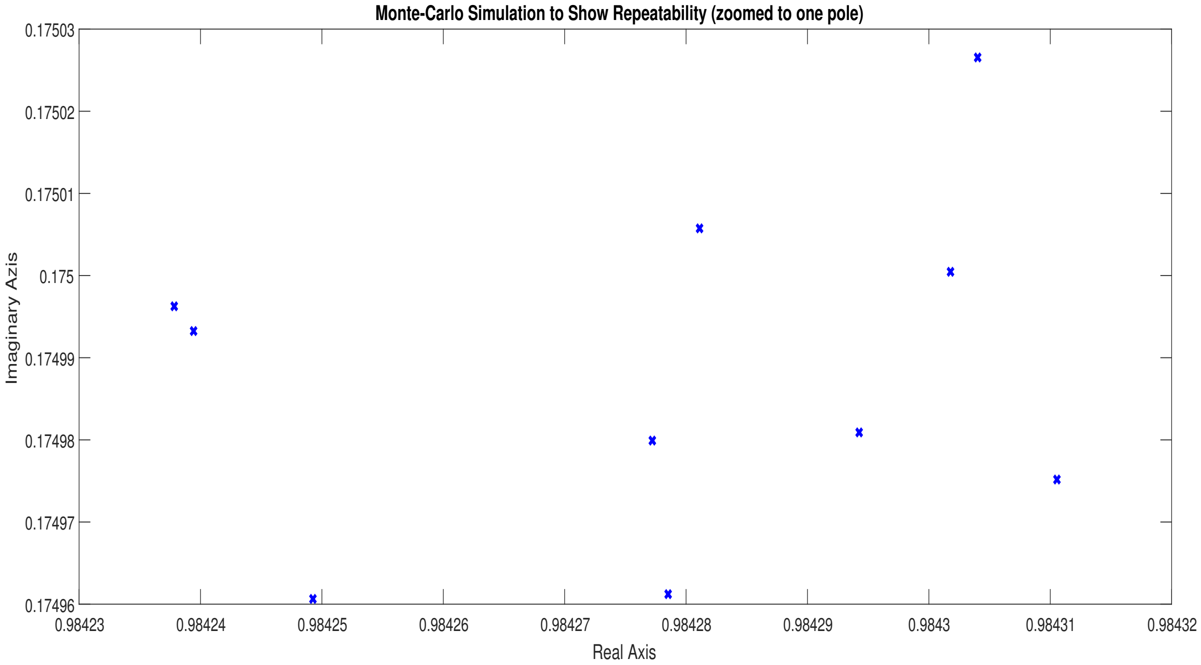

Figure 4-9: Plot of poles of the estimated system for 10 iterations (zoomed).

4-11 represents the estimation of the imaging cantilever at a noise level of 10dB. This can be attributed to significant effect of noise at higher frequencies. Signal averaging while acquiring the experimental signal during TM-AFM ensures that the SNR is always around the acceptable levels.

The estimation of the imaging cantilever is complete only when the transfer between the imaging cantilever deflection and the dither signal is obtained. This can not be obtained by using the algorithm used to estimate the transfer between deflection of imaging cantilever and tip-sample interactions since the frequency content of the dithering signal is very poor. To estimate this transfer function a sweep signal is used to dither the imaging cantilever in free air. A chirp signal with frequencies between $30kHz$ and $2MHz$ is used to deflect the imaging cantilever. With a good input and output signal, the well established PI-MOESP [14] method is used to estimate the transfer between the deflection signal of the imaging cantilever and the dithering signal. Applying the PI-MOESP method to estimate the transfer between deflection and the tip-sample interactions yields very poor results. Detailed working principle of PI-MOESP is explained in **APPENDIX**.

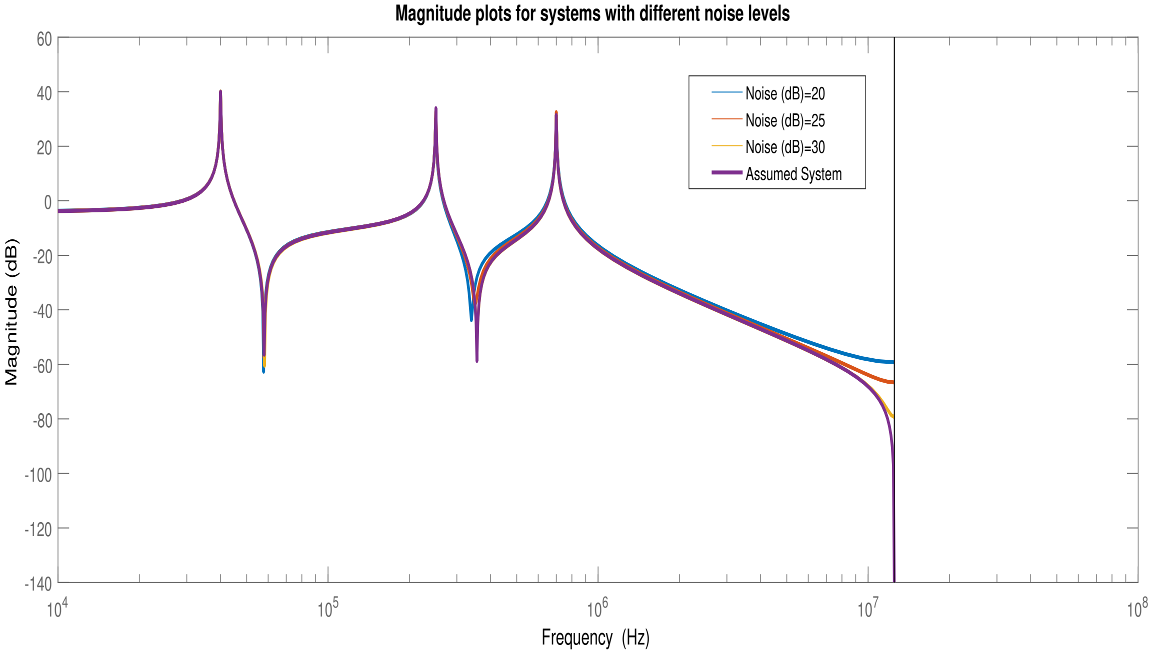

Figure 4-10: Comparison of Bode plot of the estimated system at different noise level.

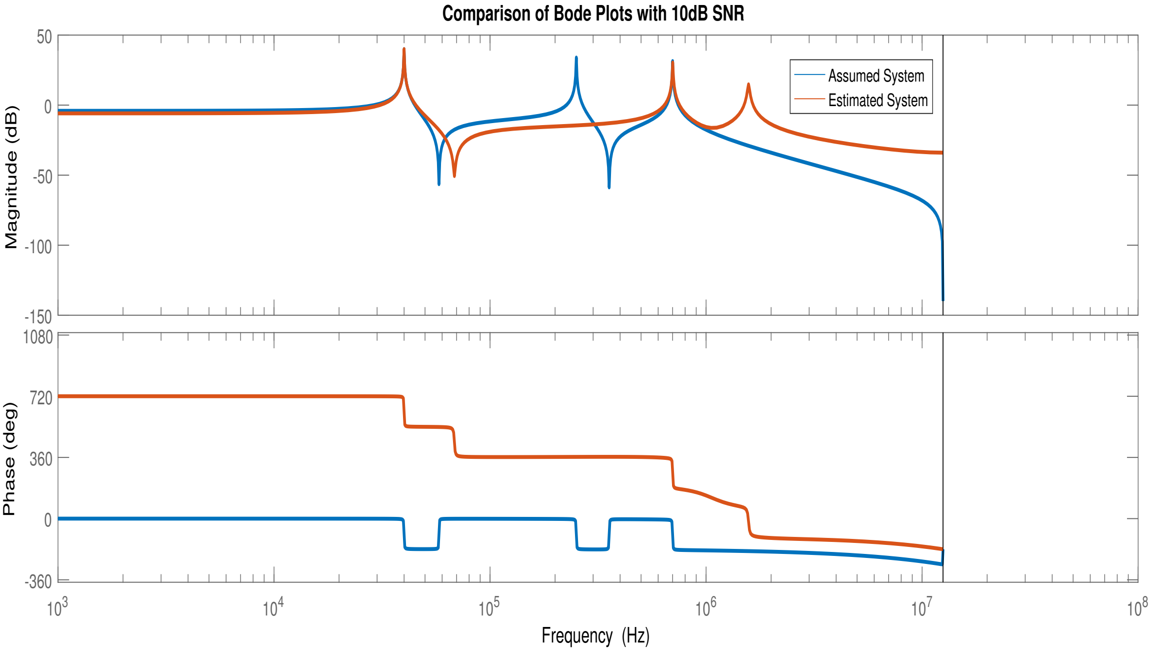

Figure 4-11: Comparison of Bode plot of the estimated system at noise of 10dB.

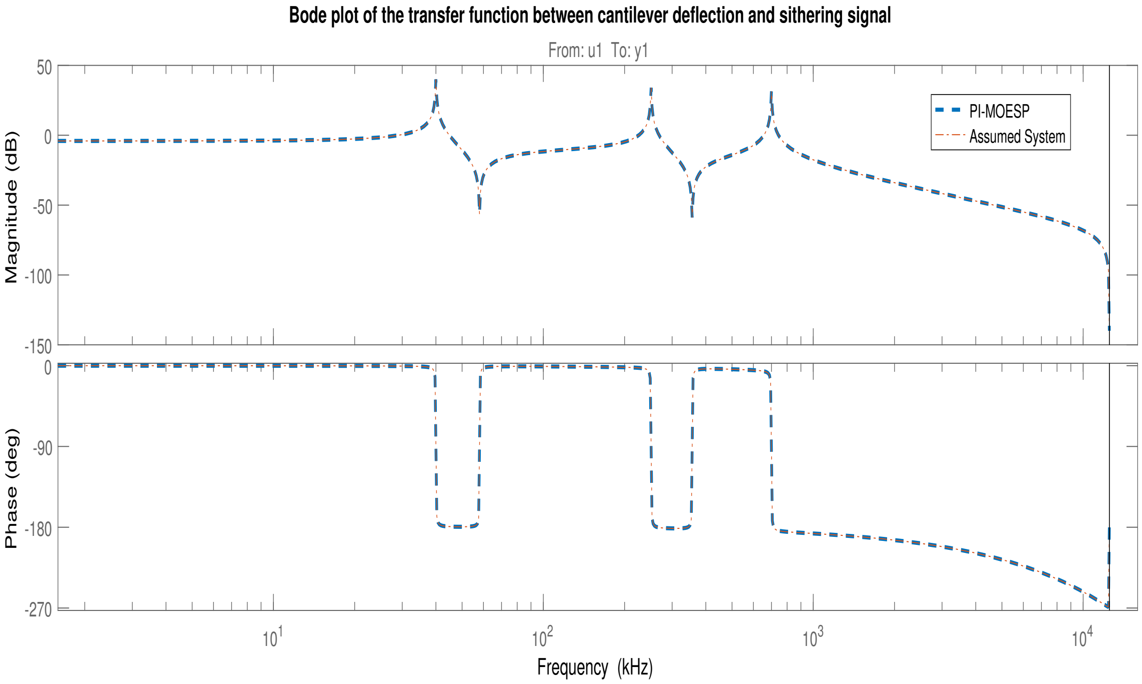

Figure 4-12: Comparison of Bode plot of the estimated transfer between deflection signal and the dithering signal using PI-MOESP.

4-2 Results from Experimental Data

With the successful application of the algorithm on simulated data, the algorithm presented in the previous chapter is tested on experimental data. Experimental setup similar to the one shown in Figure 3-1 is used. A dynamically tuned cantilever with a fundamental frequency of about $52kHz$ is used as the imaging cantilever. A Dynamically tuned cantilever as shown in 4-13 is designed by slightly altering the geometry of rectangular cantilevers to tune the higher bending modes with respect to the fundamental mode [9]. The resonance of higher modes of a rectangular cantilever are not integer multiples of the fundamental resonance and hence are not excited by the tip-sample interactions. By passively altering the geometry of the cantilever, the frequency of the higher bending mode is brought close to an integer multiple of the fundamental frequency. This way, the higher bending mode is excited by a component of the tip-sample interactions. For this thesis a cantilever with resonance frequency of second bending mode equal to 6 times its fundamental frequency is used.

Bruker Fastscan-A probe with a resonance frequency of about $1.25MHz$ is used as the sensing cantilever. Thus with this combination of imaging and sensing cantilevers, nearly 25 harmonics of the tip-sample interactions can be captured. Before beginning the estimation process, a mass spring damper model for the sensing cantilever needs to be estimated. For this purpose, the cantilevers need to be calibrated. The procedure used in [1] to calibrate a rectangular cantilever, is used to calibrate a dynamically tuned cantilever in this case.

The first step of the calibration procedure involves estimating the spring constant of the imaging cantilever. This is done by using the thermal tune method [39, 40].The basic physics

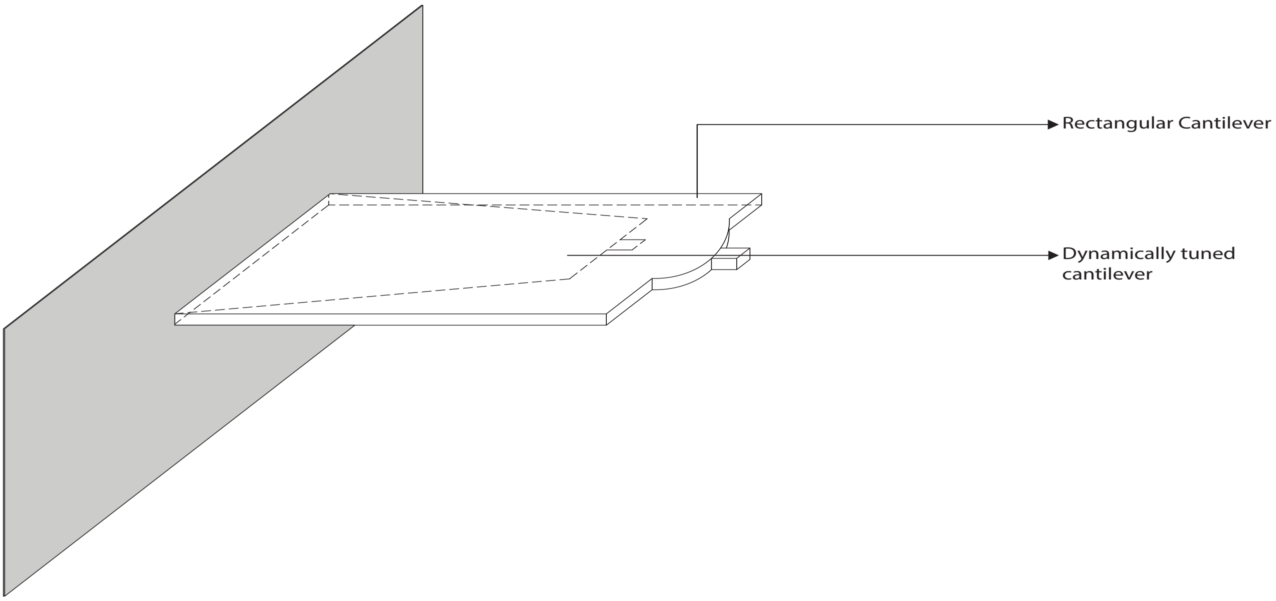

Figure 4-13: Schematic representation of a dynamically tuned cantilever.

behind this method is the equi-partition theorem, which states that at thermal equilibrium the total energy is equally shared among its various form. A harmonic oscillator in equilibrium will always oscillate in response to thermal noise with a hamiltonian (H) given by

$$H = \frac{1}{2} m \omega_0^2 q^2 + \frac{p^2}{2m}$$

with ω_0 being the fundamental resonance frequency, q being the displacement of cantilever tip, m being the cantilever mass and p the momentum of the cantilever. By equi-partition theorem each energy term contributing to the hamiltonian is equal to $\frac{k_b T}{2}$ where k_b is the Boltzmann's constant and T the ambient temperature. With the knowledge that spring constant $k = \omega_0^2 m$ we have

$$k = k_b T / < q^2 >$$

Since the higher bending modes of a cantilever are stiffer than the fundamental mode, the contributions of the higher bending modes to the deflection of the cantilever due to thermal fluctuations can be neglected and the spring constant can be estimated using the area under the first resonance peak due to thermal vibrations.

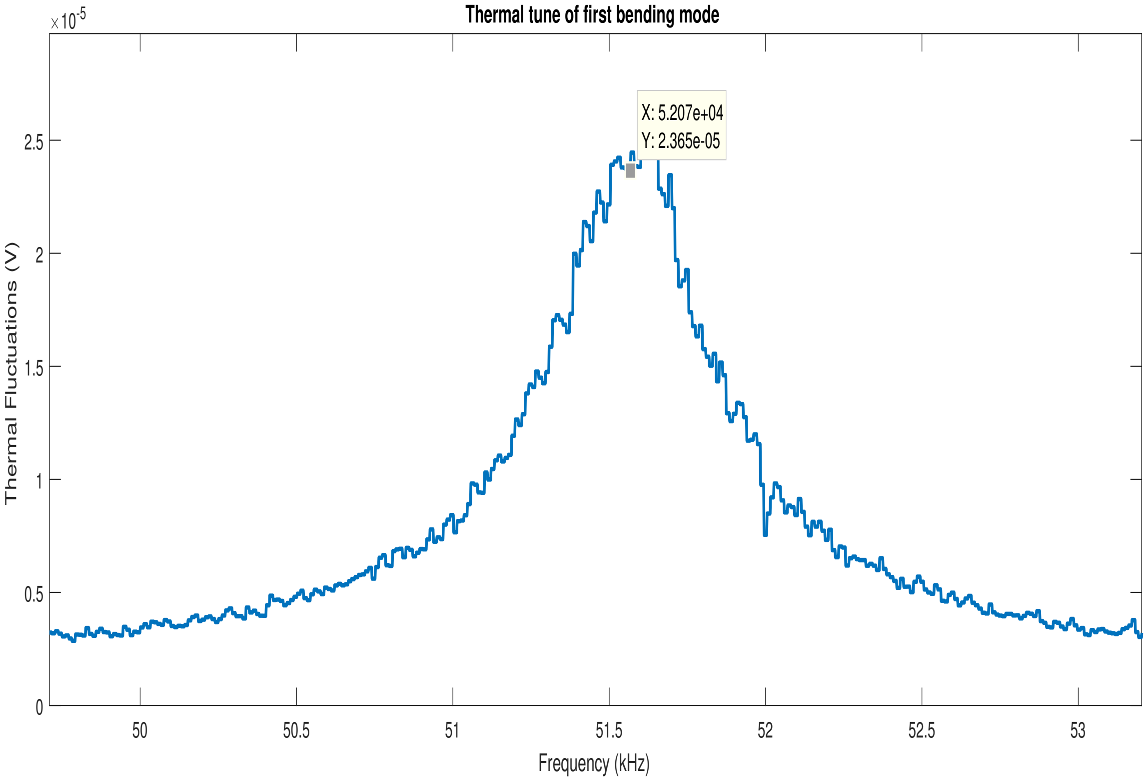

Figure 4-14: First resonance peak obtained through thermal fluctuations.

Figure 4-14 depicts the first resonance peak obtained through thermal fluctuations. This information is used to determine the effective spring constant of the cantilever. Using the thermal fluctuations the effective spring constant of the cantilever is estimated to be $0.91Nm^{-1}$.

Having calibrated the spring constant of the imaging cantilever, the next step of the calibration process is to estimate the sensitivity of the deflection measurement system. For this purpose the imaging cantilever is engaged with a sapphire crystal placed on the sample stand. Since the stiffness of the sapphire crystal is very large when compared to that of the imaging cantilever, the deflection of the crystal when engaged with the imaging cantilever is considered 0. The imaging cantilever is engaged with the sapphire crystal in contact mode and when in contact, the z-stage (shown in the experimental set-up) is moved by a known distance (say $x\ nm$). The sensitivity of the deflection signal is obtained by calculating the slope of the linear compliance region in the deflection vs distance graph of the deflection signal.

Figure 4-15 represents the plot of the movement of the imaging cantilever with z-stage movement in contact mode. The z-stage is moved by $60nm$ and the corresponding deflection of the imaging cantilever is acquired. Since the sapphire crystal has a very high stiffness, it is reasonable to assume that the imaging cantilever moves by $60nm$ as well. Using this information the deflection sensitivity of the imaging cantilever is found to be $382nmV^{-1}$.

After calibrating the imaging cantilever, it is now engaged with the surface of the sensing cantilever, close to its probe tip. Similar to the previous case, the set-up is ramped by moving the z-stage by a known value. With the knowledge of the deflection sensitivity of the imaging cantilever, the deflection of the imaging cantilever can be obtained. The difference between z-stage movement and the deflection of the imaging cantilever is the amount by which the sensing cantilever is deflected. With this knowledge the spring constant of the sensing

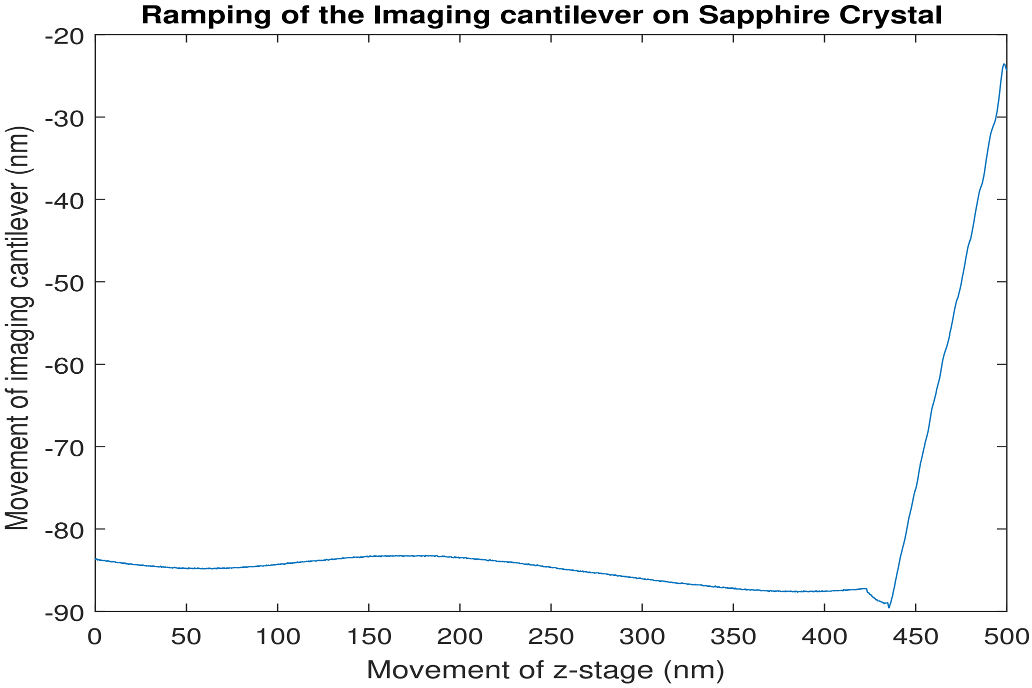

Figure 4-15: Movement of the Imaging Cantilever with z-stage movement.

cantilever is found to be 87.5 Nm^{-1} and the deflection sensitivity of the sensing cantilever is measured to be 109.9 nmV^{-1}.

Figure 4-16 and 4-17 represent the deflection versus z-stage movement plots of deflection of imaging cantilever and the deflection of the sensing cantilever respectively. From these plots the spring constant and the deflection sensitivity of the sensing cantilever is calculated.

With knowledge of the spring constant, resonance frequency and the Q-factor of the sensing cantilever, its dynamics can be modeled by using a simple mass-spring-damper system in the same way as explained earlier. Resonance frequency and the Q-factor are obtained from the thermal fluctuations of the cantilever and are found to be $1.25MHz$ and 250 respectively. The dynamics of the sensing cantilever in continuous domain can be represented by

$$\begin{aligned} \dot{x_s} &= \begin{bmatrix} \frac{-c_s}{m_s} & \frac{-k_s}{m_s} \\ 1 & 0 \end{bmatrix} x_s + \begin{bmatrix} \frac{1}{m_s} \\ 0 \end{bmatrix} U_{ts} + w_s \\ y_s &= \begin{bmatrix} 1 & 0 \end{bmatrix} x_s + v_s \end{aligned} \tag{4-4}$$

with the modal parameters having the same meaning as before. A zero order hold discretization is used to discretize the system at a sampling frequency of $250MHz$. The experiments are performed at three different frequencies being $52033Hz$, $52090Hz$ and $52847Hz$. In order to reduce the noise in the measured data, the signals are averaged over 50 measurements. Figure 4-18 compares the recorded data obtained by averaging and that without averaging. This clearly shows that signal averaging increases the SNR of the acquired signal.

In a similar way as in the simulations case, the number of harmonics of the tip-sample interactions is decided by observing the FFT of the deflection of the sensing cantilever.

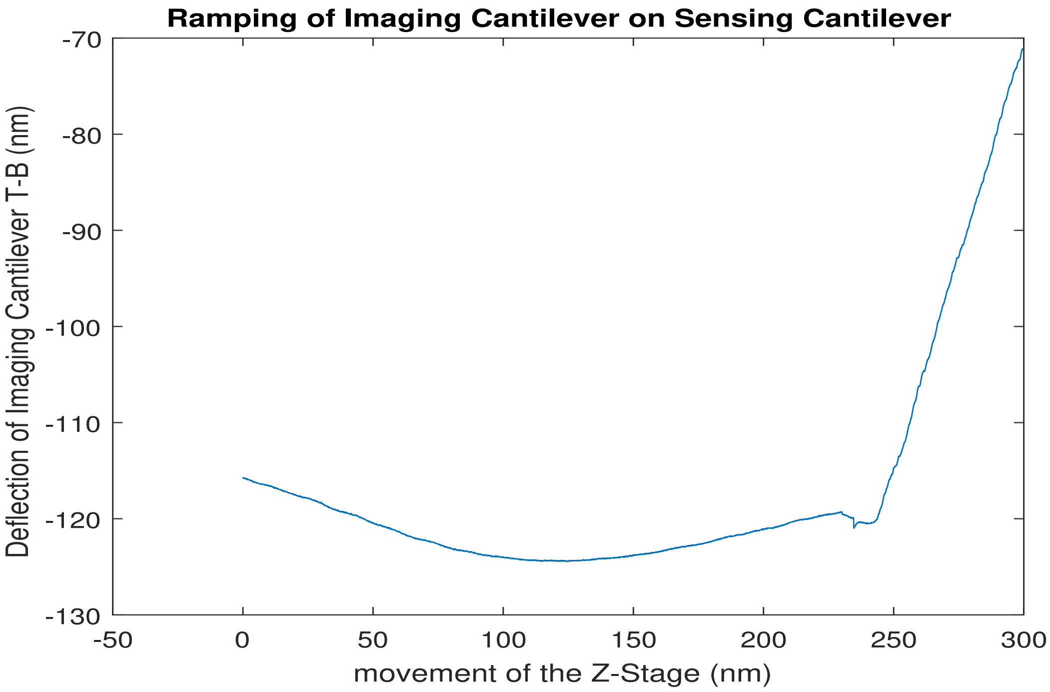

Figure 4-16: Movement of the Imaging Cantilever with z-stage movement (T-B signal).

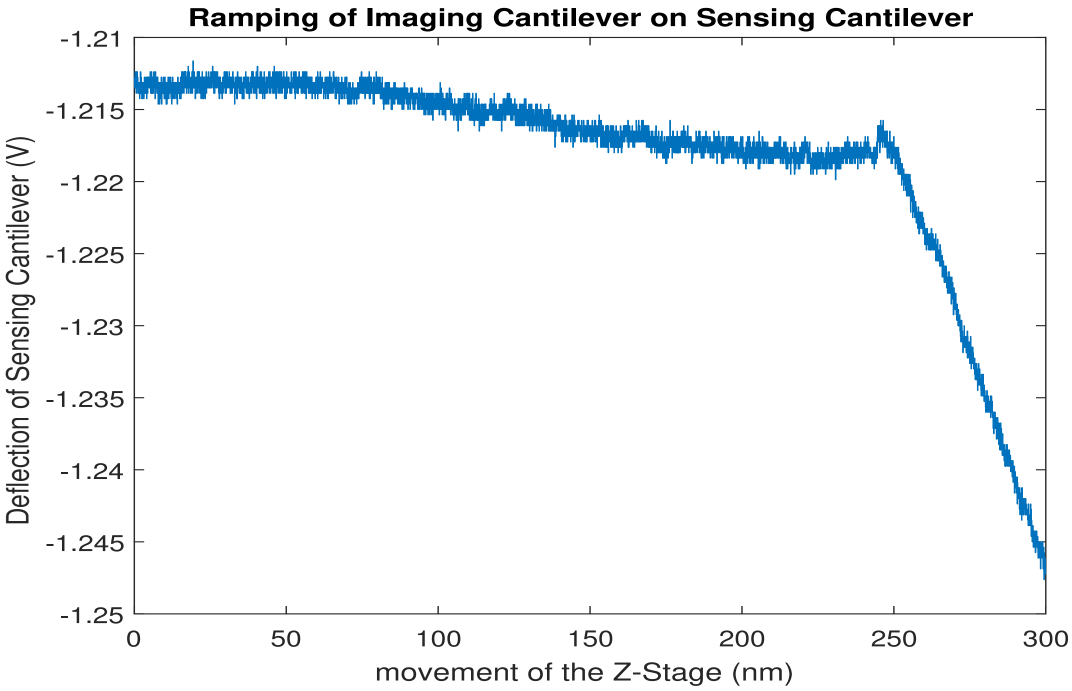

Figure 4-17: Movement of the Sensing cantilever with z-stage movement.

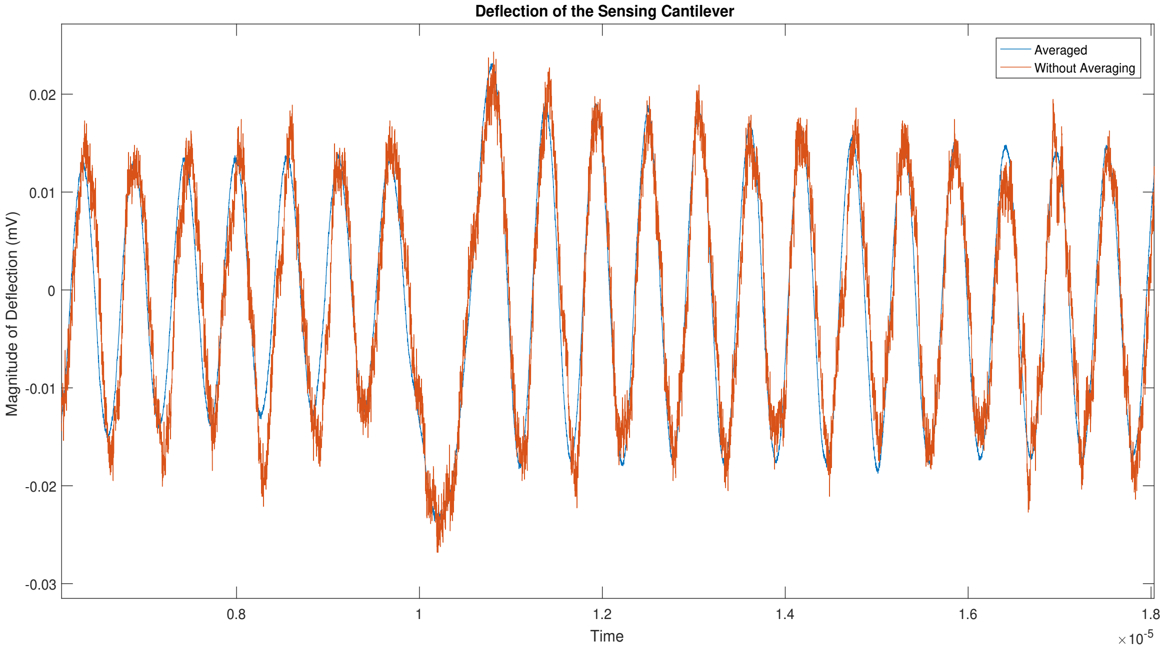

Figure 4-18: Movement of the Sensing cantilever with z-stage movement.

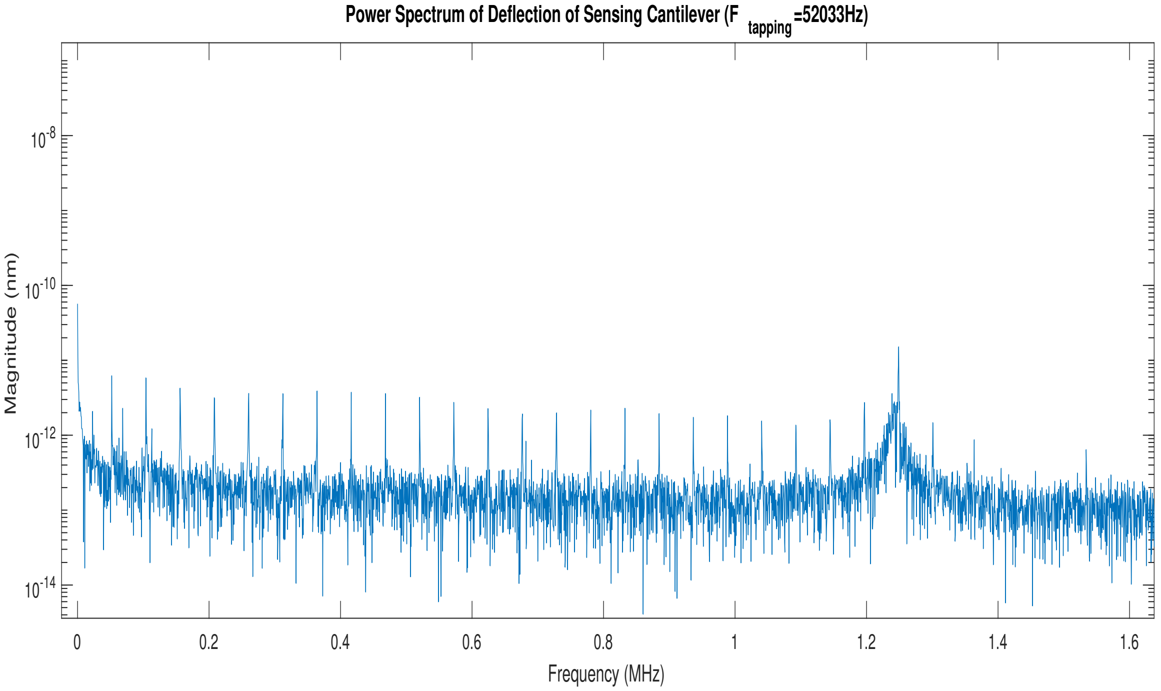

Figure 4-19: Power Spectrum of Deflection of Sensing Cantilever (52033 Hz).

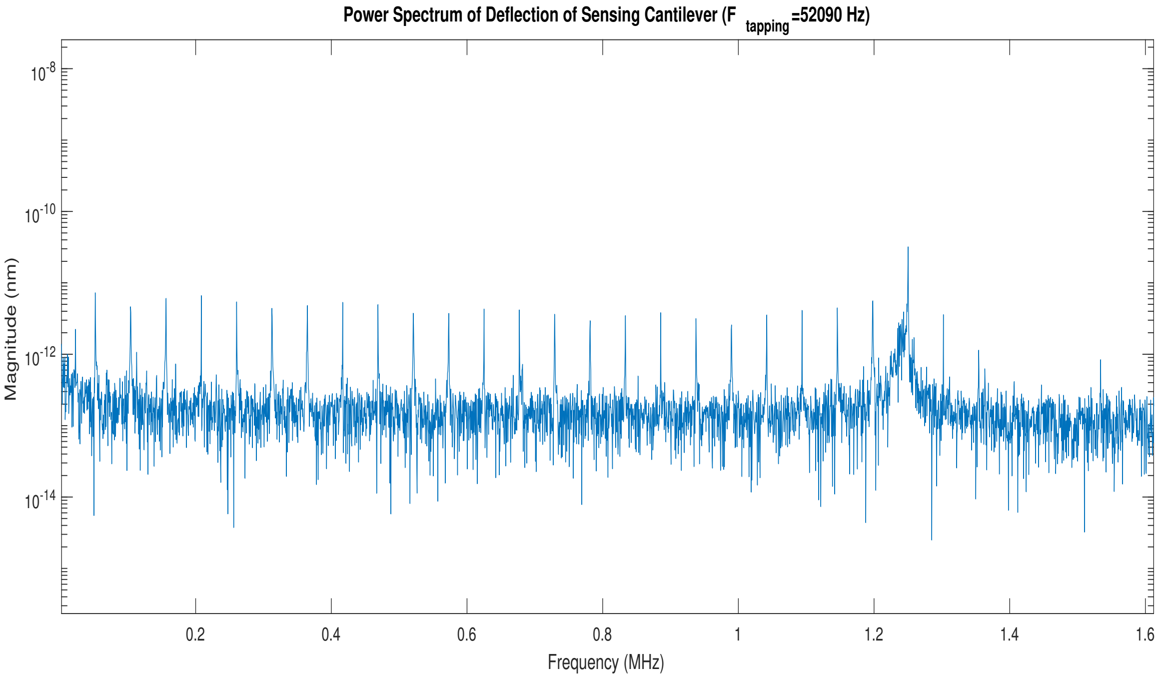

Figure 4-20: Power Spectrum of Deflection of Sensing Cantilever (52090 Hz).

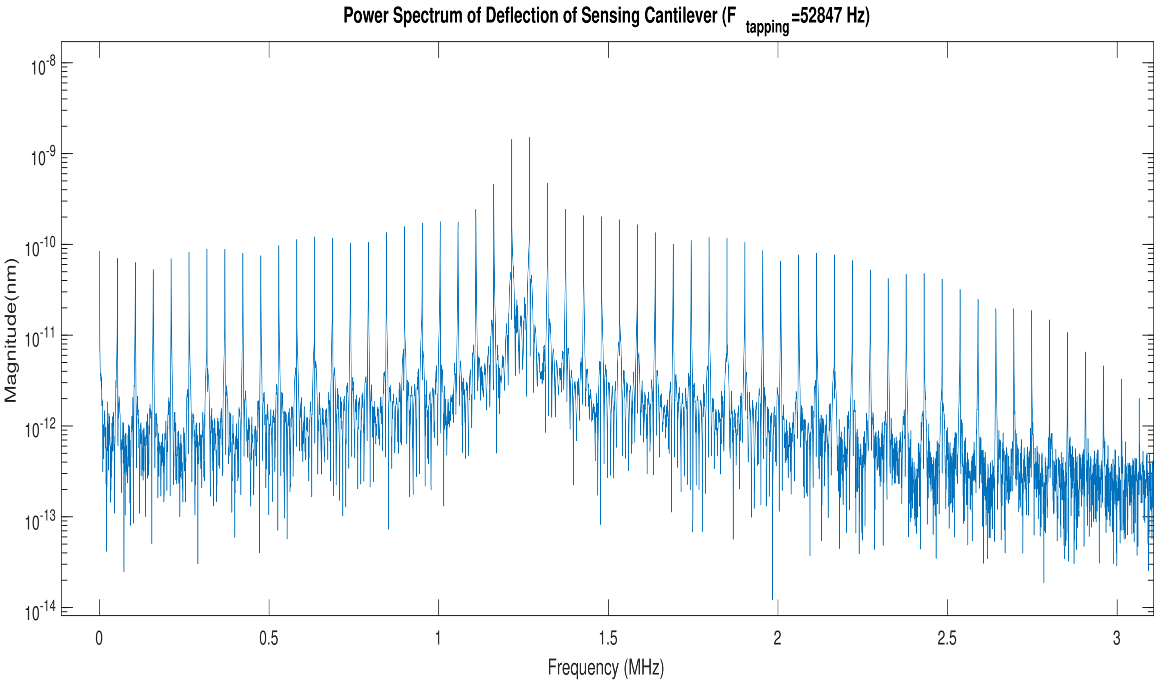

Figure 4-21: Power Spectrum of Deflection of Sensing Cantilever (52847 Hz).

Figure 4-19,4-20 and 4-21 clearly depicts the contribution of the higher harmonics of the tip-sample interactions for each of the three dithering frequencies. Thus the number of harmonics of the tip-sample interactions to be estimated for each of the three tapping frequencies is chosen to be 25, 25 and 50 respectively. The tip-sample interactions are estimated in the same way as in the simulations case.

Figure 4-22 and 4-23 shows the estimated tip-sample interactions at the various tapping frequencies. The estimated signals seem to follow a similar trend followed by tip-sample interactions as estimated in earlier works. Figure 4-24 portrays the estimated tip-sample interactions superimposed over its corresponding sensing cantilever deflection signal. The deflections signal seems to lag the tip-sample interactions by a small value. This is due to the phase addition by the sensing cantilever to the tip-sample interactions.

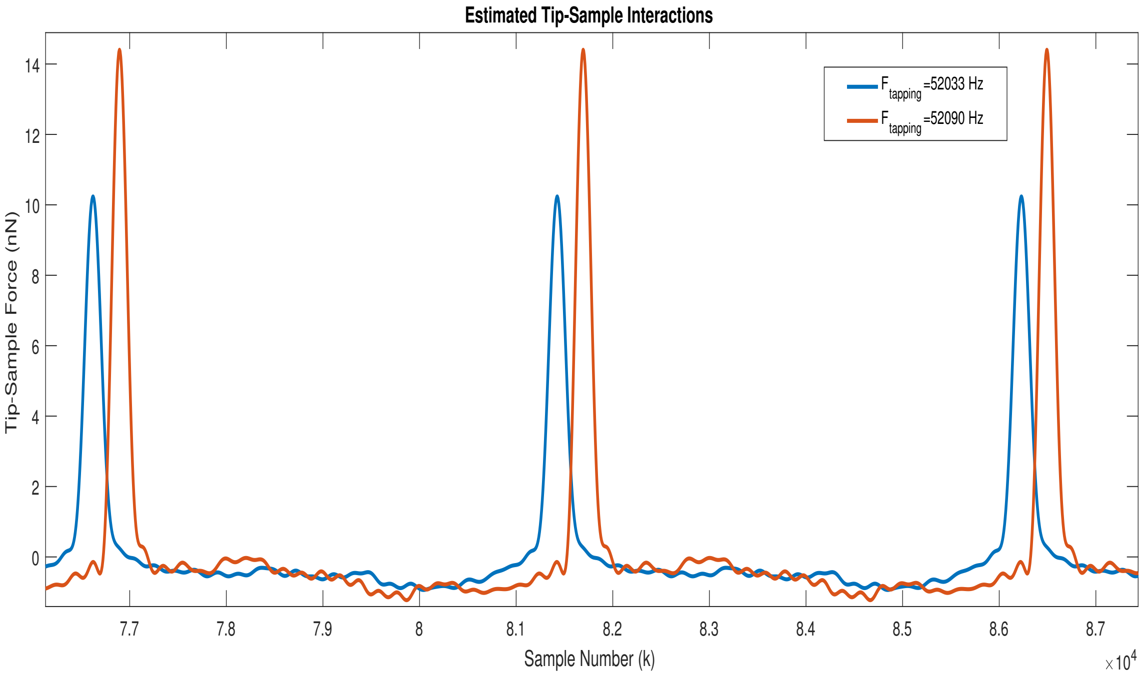

Figure 4-22: Estimated Tip-Sample Interactions at 52033 Hz and 52090 Hz.

To validate the estimation of the tip-sample forces, it is compared with the tip-sample interactions obtained by using the force sensitivity method. The author in [1] estimates the tip-sample force by scaling the deflection of sensing cantilever with force sensitivity. The author filters the time-series signal using a low pass filter, to remove the frequency components that are above the resonance frequency of the sensing cantilever. By doing so, information about the harmonics that are above the resonance frequency of sensing cantilever is lost. Traditionally the tip-sample forces are directly scaled using the force sensitivity value. The force sensitivity is obtained as a product of deflection sensitivity of the sensing cantilever and its spring constant. This assumes that the attenuation of the tip-sample forces due to sensing cantilever is constant throughout. However this assumption is not true for harmonics that are above the resonance frequency of the sensing cantilever due to its dynamic characteristics.

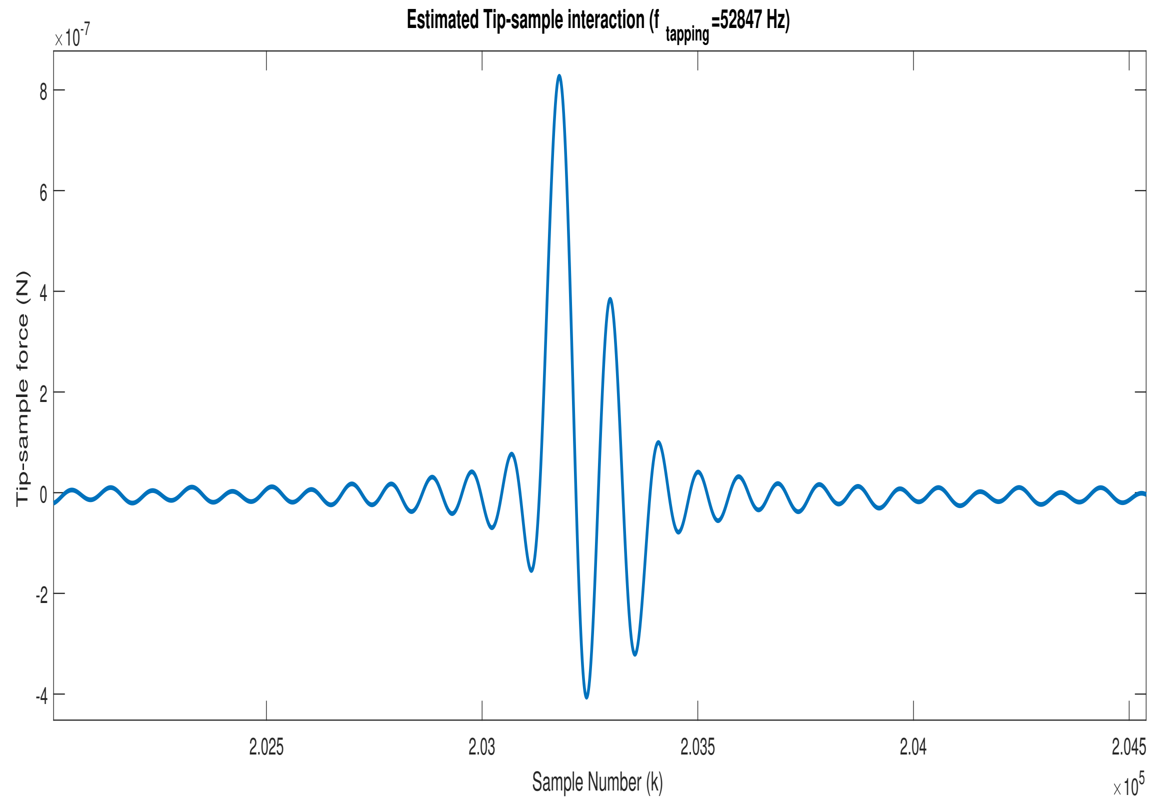

Figure 4-23: Estimated Tip-Sample Interactions at 52847 Hz.

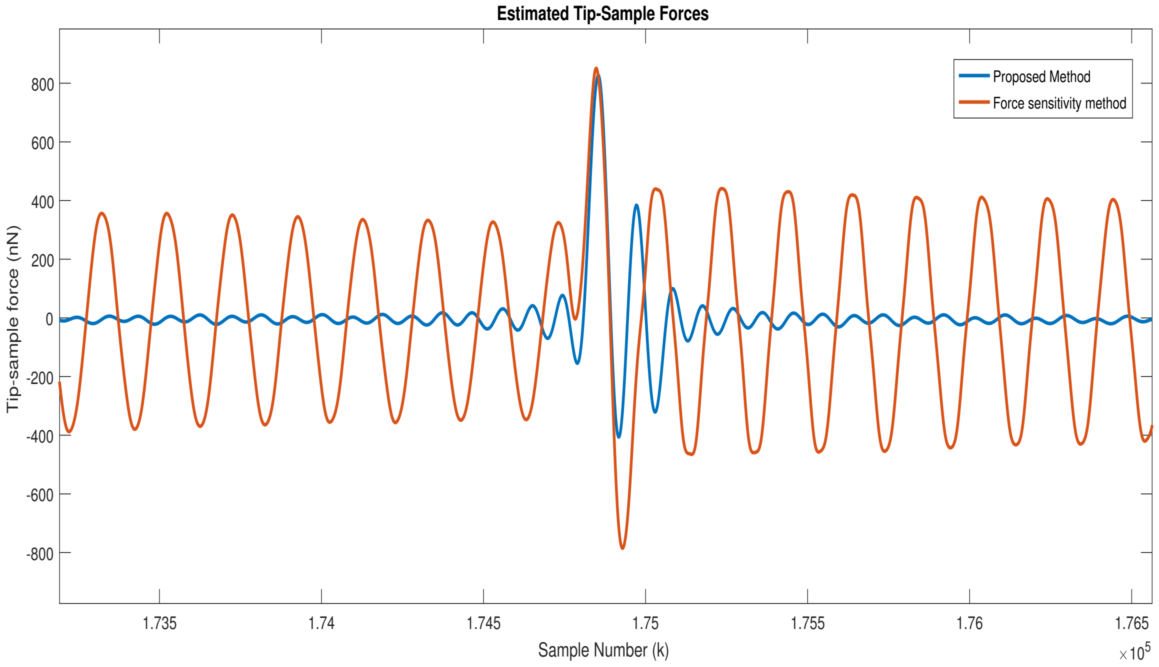

Figure 4-25: Comparison between estimated tip-sample interaction using proposed method and force sensitivity method $(F_{tapping} = 52847Hz)$.

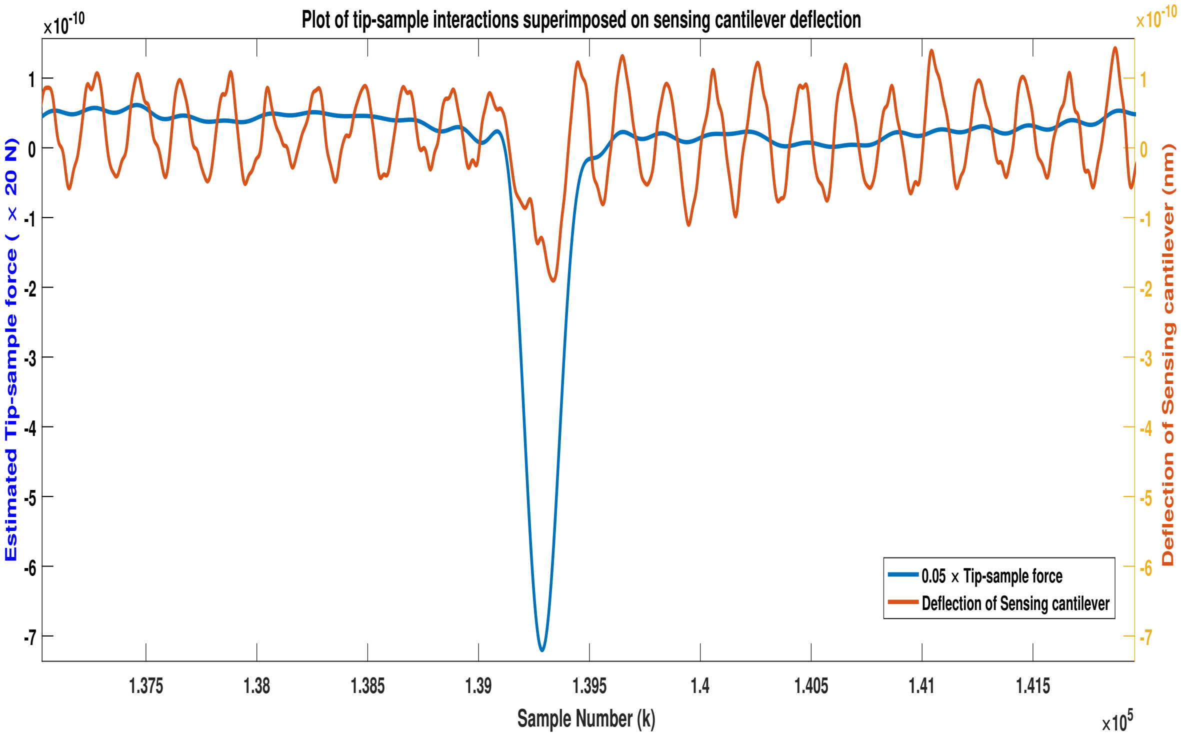

Figure 4-24: Estimated Tip-Sample Interactions superimposed with the corresponding deflection signal (52090 Hz)

Figure 4-25 compares the tip-sample forces estimated using the developed algorithm with the force estimated using force sensitivity method. The force sensitivity for the particular experiment is found out to be $9633 nNV^{-1}$. The comparison shows that the proposed method takes into account the dynamics of the sensing cantilever in estimating the tip-sample interactions. Also, the peak force estimated using the two methods are close to each other, thus proving the effectiveness of the proposed method. Moreover, the closeness of the two signals suggests that the model of the sensing cantilever is accurate.

Having estimated the tip-sample interactions, the frequency response at various frequencies is obtained in the same way as outlined in the previous chapter. For estimation using simulations it was assumed that the contributions of the tip-sample interactions and the dithering signal at fundamental frequency are equal, i.e the input matrix in the state space representation of the imaging cantilever is the same for both the inputs. In reality the input matrices are not identical and hence an extra experiment is performed to obtain the response of the cantilever to the dithering signal in free air at different operating frequencies. With this knowledge, the frequency response at the fundamental frequency due to tip-sample interactions can be calculated using simple linear equations. This frequency response estimate is further used to determine the transfer function of the imaging cantilever. The order of the system is decided based upon the frequency spectrum of the deflection of the imaging cantilever.

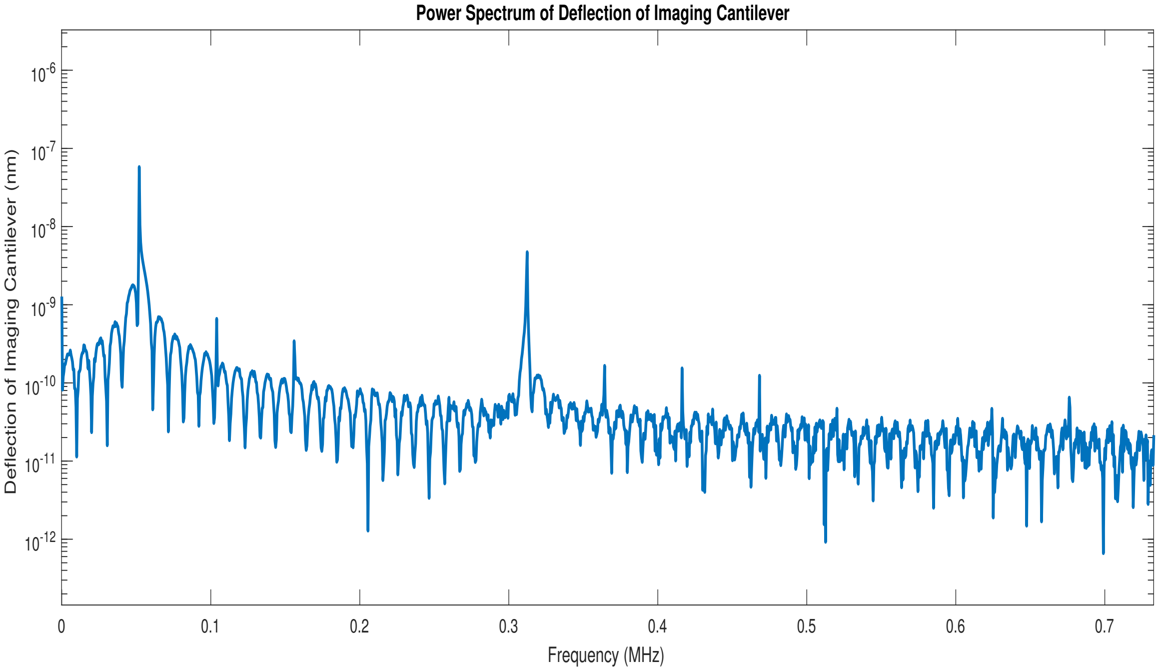

Figure 4-26: Frequency Spectrum of Deflection of Imaging cantilever ($f_{tapping} = 52033Hz$)

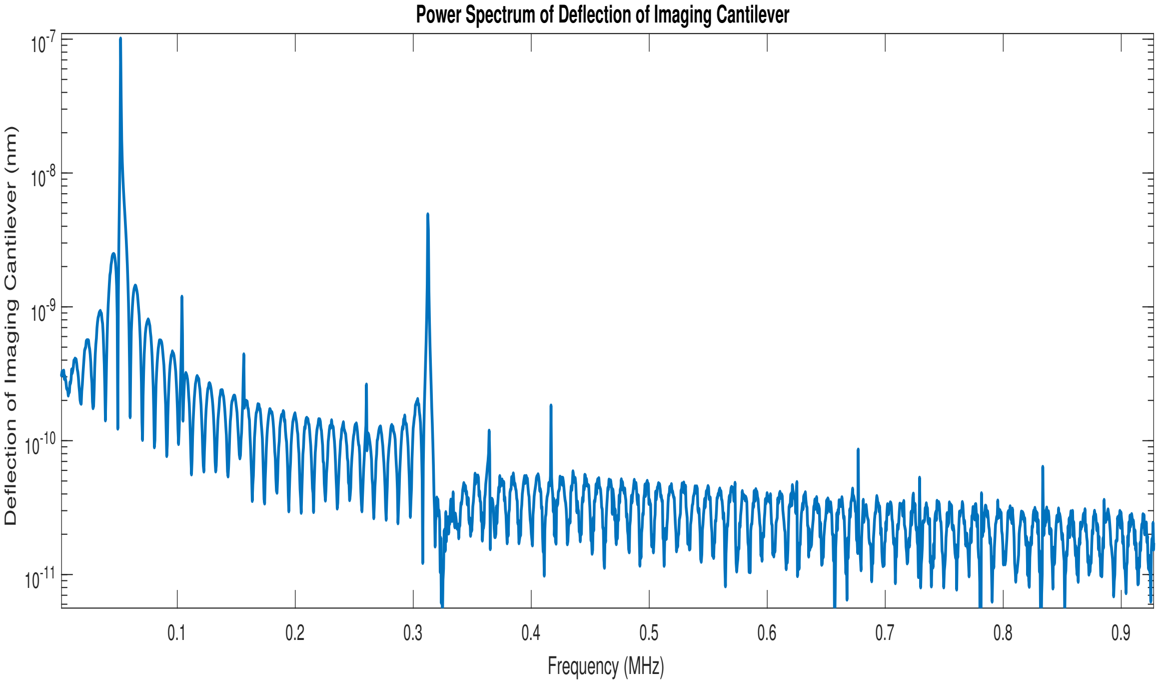

Figure 4-27: Frequency Spectrum of Deflection of Imaging cantilever ($f_{tapping} = 52090Hz$)

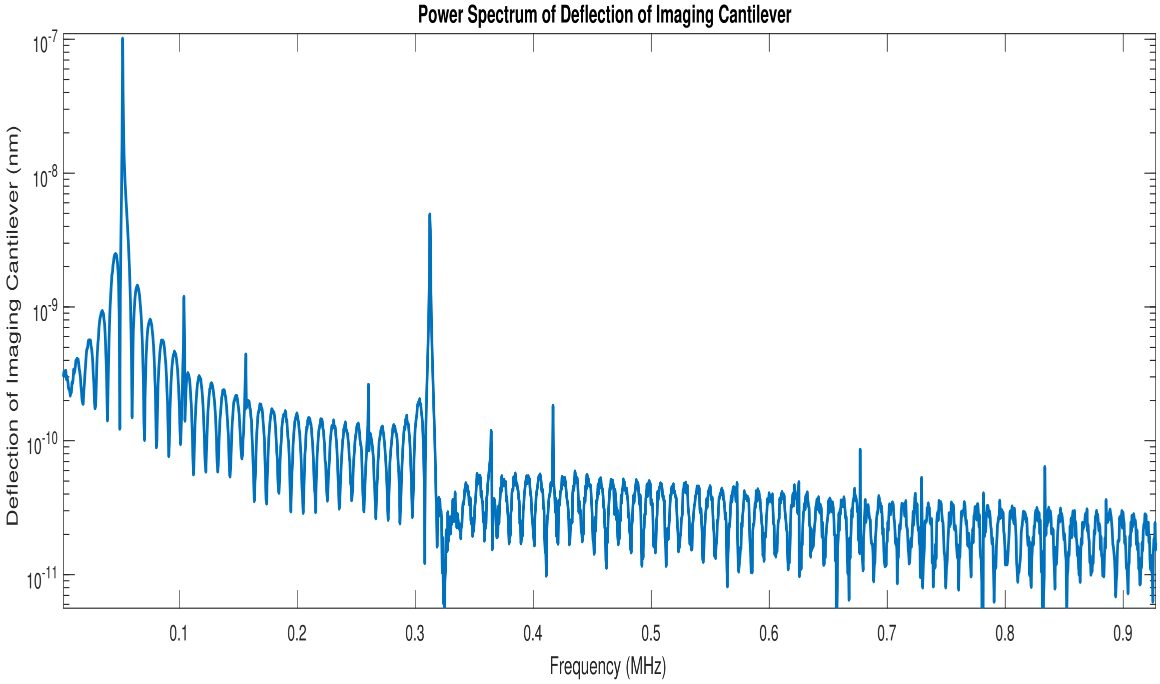

Figure 4-28: Frequency Spectrum of Deflection of Imaging cantilever ($f_{tapping} = 52847Hz$)

Figure 4-26 depicts the frequency spectrum of the deflection of the imaging cantilever. It is evident from the frequency spectrum that the first two bending modes (f_0 and $6f_0$) are excited by the input signals. The point of actuation (tip-sample forces) and the sensor (OBD) are at the same place on the cantilever. Thus, the system between tip-sample interactions and the imaging cantilever deflection must be collocated. Also, from the figure small contributions due to second and third harmonics of the tip-sample interactions to the deflection of the imaging cantilever can be seen. In between the 3^{rd} and the 6^{th} harmonic the spectrum is flat which suggests that the zero of the system lies in between these frequencies. Similarly looking at Figures 4-28 and 4-27 is can be concluded that the complex zero lies between $158.5kHz$ and $260kHz$.

Having estimated the frequency response complex numbers, the transfer function between the estimated tip-sample interactions and the imaging cantilever deflection is estimated using the algorithm outlined in the previous chapter. Using the magnitude of the frequency response as a weighting vector results in a system whose bode plot is represented by Figure 4-29. The estimated system has its poles at the same frequencies as obtained through the thermal fluctuations of the imaging cantilever. The estimate of the zero is at a frequency in between the third and the sixth harmonic of the fundamental frequency but is not visible from the bode diagram. To improve the estimate of the zeros the weights at frequencies corresponding to the 4^{th} and the 5^{th} harmonics need to be increased. A weight of 2700 is imposed at these frequencies. Figure 4-30 depicts the system estimated with a modified weighting vector. A collocated system with a complex zero in between the 3^{rd} and 6^{th} harmonics is estimated as expected. Also a steep roll-off can be seen at high frequencies. Figure 4-26 validates this fact,

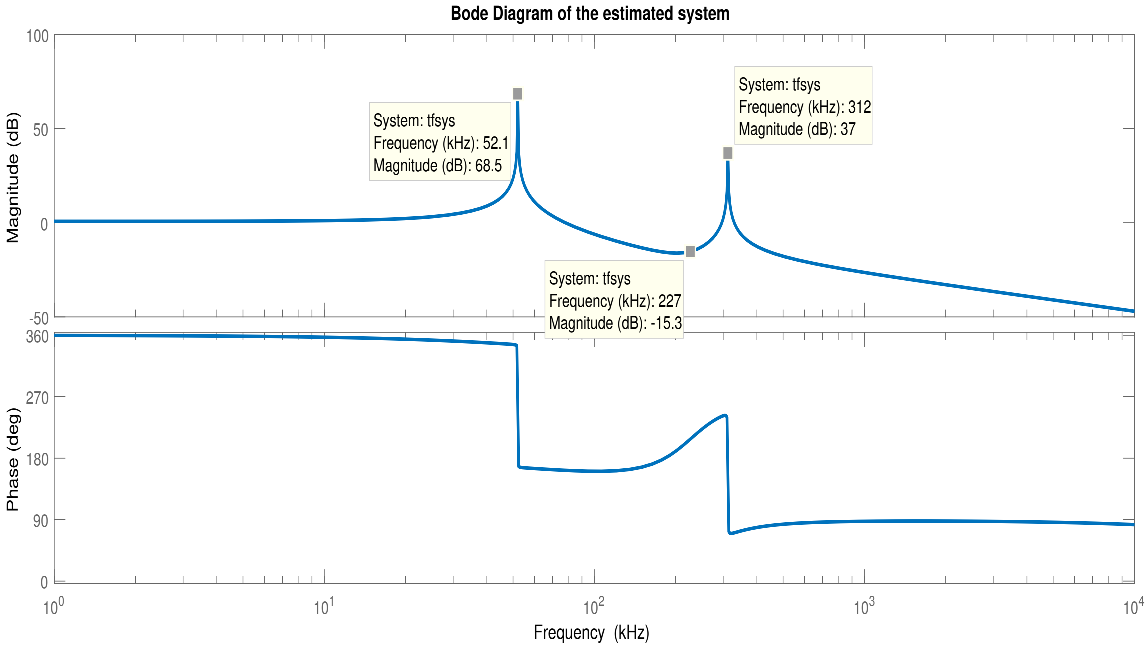

Figure 4-29: Bode plot of the Estimated system with magnitude of frequency response as weighting matrix.

as the contributions of higher harmonics to the deflection of the imaging cantilever fade away after the 10^{th} harmonic.

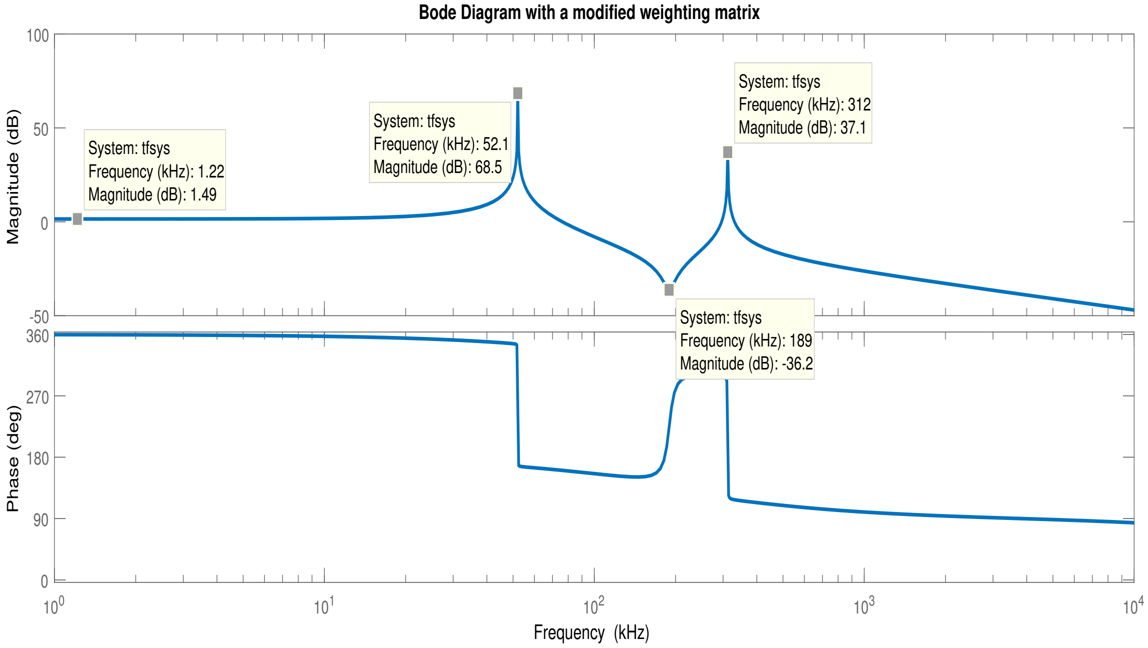

Figure 4-30: Bode plot of the Estimated system with weighting matrix $W(\omega_k)$.

Bending Mode	ω_n from Spectrum Analysis	Estimated ω_n
1	52.072kHz	52.058 kHz
2	312.34 kHz	312.33 kHz

Figure 4-14 and 4-31 represent the thermal fluctuations of the 1^{st} and 2^{nd} bending modes of the imaging cantilever. From the figures it can be seen that the resonance frequencies of the estimated system match with the resonance frequencies obtained by thermal tune method but with a very small error. This validates the supremacy of the developed algorithm. From the bode plot of the estimated system it can also be noticed that the static region has a magnitude of $1.49dB$ (1.18 in linear scale). This value is very close to the reciprocal of the spring constant, which is equal to 1.09. This establishes the superiority of the estimation process.

The transfer function between the dithering signal and cantilever deflection can be estimated using input-output data obtained by dithering the imaging cantilever in free air. A sweep signal can be used to dither the cantilever to ensure that the input is persistently exciting. The system transfer between the deflection and dithering signal can be estimated using PI-MOESP subspace identification technique.

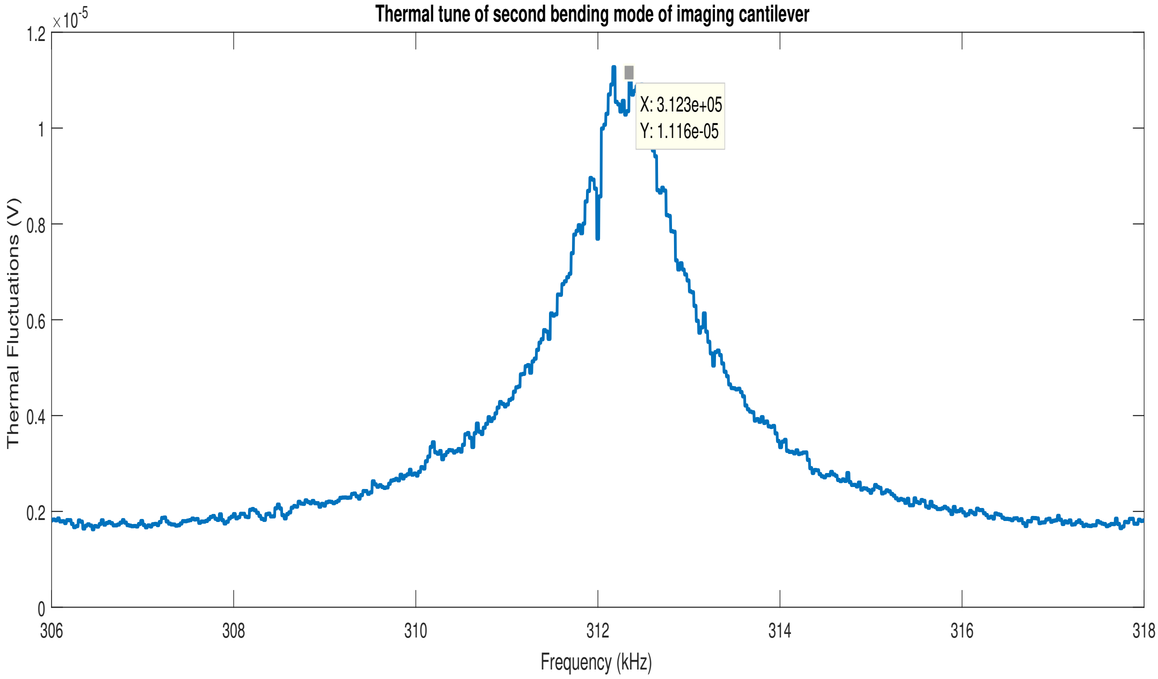

Figure 4-31: Thermal tune of second bending mode of imaging cantilever.

Chapter 5

Conclusions

In the previous chapters an outline of atomic force microscope is presented. The various problems associated with the present set ups are discussed in detail and it is concluded that it is important to include the dynamics of the cantilever while estimating the tip-sample forces. This way higher harmonics of the cantilever, which contain crucial information about several forces, can be estimated. The estimation of the dynamics of the cantilever is not straight forward since placing a sensor at the point of tapping in TM-AFM is impossible to directly measure them. Thus the thesis aims at developing an algorithm to estimate a mathematical model for the probe of an AFM with an unknown input.

An experimental set up as proposed in [1] is used to obtain the experimental data for the thesis. Since the static region of the sensing cantilever is extremely large, its dynamics are modeled using one bending mode of the cantilever. The sensing cantilever is modeled as a 2-DOF mass spring damper system. It is noticed that averaging the signal while acquiring them reduces the noise levels in the signal and produces a nearly noiseless data. With prior knowledge about the cantilevers, the periodic nature of the tip-sample interactions in TM-AFM is exploited to reconstruct them using inversion at specific frequencies. The estimate of the tip-sample interactions is validated using the force sensitivity method and found to estimate the peak tapping force accurately.

With the estimation of the tip-sample interactions, the frequency response of the imaging cantilever is obtained, again by solving a set of linear equations. The transfer function between the tip-sample interactions and deflection of imaging cantilever is estimated by using S-K iterations and curve fitting. From the estimation procedure applied to simulated data, it is found that the estimation procedure works well and the estimated system fits well with the signal generating model. It is also noted that the estimation procedure performs well up to 20 dB noise levels above which the performance of the algorithm starts decreasing. It is also concluded that tapping at three different frequencies improves the performance of the algorithm when compared to estimation using data acquired at one working frequency .

The estimation with the experimental data does not look as simple as for the simulations case. This can be attributed to the non linearities or some un-modeled dynamics of the cantilever. Although with proper selection of the weighting matrix it is seen that the poles, zeros and the steady state response are estimated accurately using the proposed algorithm.

Further this algorithm can be combined with the regularized Kalman filter [11] to estimate the tip-sample interactions directly when the cantilever is engaged in tapping mode with a sample surface. This algorithm can also be used to determine the modal parameters from the knowledge of poles of the estimated system.

As a next step, to further improve the estimation process, non- linearities of the sensing and imaging cantilever can be modeled. This can also improve the estimate of the tip-sample interactions. Also, more tapping points can be included in the experimental procedure in order to excite the third bending mode of the cantilever.

Appendix A

Optical Beam Deflection Method

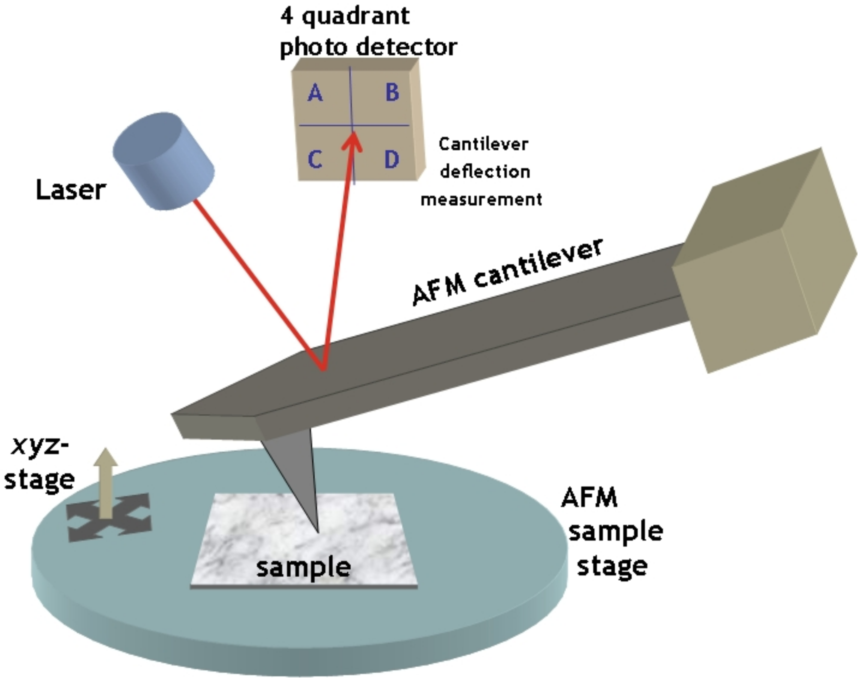

Figure A-1: Schematic of the optical beam deflection method.

Source : Open source Handbook of Nano-science and Nanotechnology [41]

Figure A-1 represents a schematic representation of the optical beam deflection (OBD) method. OBD is the most widely used method to measure AFM cantilever deflection. The sensor mainly consists of a laser and four quadrant split photo detector. A laser light of specific wavelength is reflected off the rear side of the cantilever. When the cantilever is at rest the laser spot is concentrated at the center of the photo detector, which signifies zero deflection. In TM-AFM, when the cantilever tip deflects from the set-point amplitude, the four quadrants of the photo detector receive different intensities of laser light. The photo induced current from the different photo detectors are fed into a signal conditioning circuit that produces a voltage signal that is proportional to the deflection of the cantilever. The difference in intensities between the top and bottom half of the photo detector is proportional to the deflection in the vertical direction. Similarly the difference in intensities between the left half and the right half is proportional to the deflection in the lateral direction.

$$\begin{aligned} \delta_{vertical} &\propto \frac{(A+B)-(C+D)}{A+B+C+D} \\ \delta_{lateraal} &\propto \frac{(A+C)-(B+D)}{A+B+C+D} \end{aligned}$$

With the knowledge of set point amplitude, deflection sensitivity of the photo detector and the amplifier gains, the exact deflection of the cantilever can be obtained.

Appendix B

Lock-in Amplifier

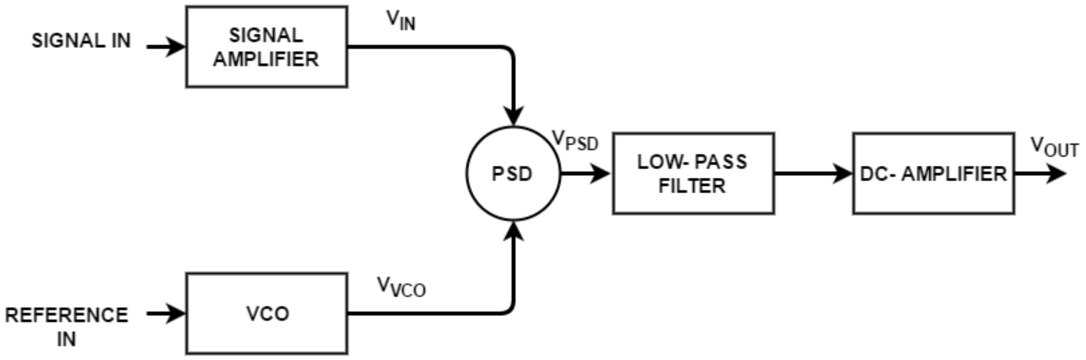

Figure B-1: Block diagram of a simple lock-in amplifier.

The basic block diagram of a lock in amplifier is represented in Figure B-1 [42]. In a nutshell, the lock-in amplifier is used to measure the amplitude (and phase) of the cantilever deflection from the feedback control signal. The PSD block in block diagram is a phase sensitive device which multiplies the control signal received from the feedback controller and the reference signal from a voltage controlled oscillator (VCO). The frequency of the reference signal is similar to the frequency input signal and this is achieved using a VCO. Suppose the control signal from the feedback electronics is $V_0 cos(\omega_0 t + \phi)$ and the reference signal be $E_0 cos(\omega_0 t)$, the output of the PSD is given as

$$V_{psd} = E_0 V_0 cos(\omega_0 t) cos(\omega_0 t + \phi)$$

From basic trignometric identities we know that a signal that is a product of two sinusoids of frequencies f_1 and f_2 can be represented as a sum of sinusoids of frequencies $f_1 + f_2$ and $f_1 - f_2$ which yields

$$V_{psd} = \frac{1}{2} E_0 V_0 (cos(\phi) + cos(2\omega_0 t + \phi))$$

An appropriately designed low pass filter is used to filter out the high frequency components. This signal is further passed through a dc amplifier to achieve necessary amplification. With known values of low pass filter gain and the DC amplifier gain, the output of the lock-in amplifier with a single PSD can be interpreted as $V_0 cos(\phi)$.

To separate the phase component from the final output, a secondary PSD with a 90° phase shifted reference input is used. The output of the combination of secondary PSD and low-pass filter combination results in $V_{psd2} = V_0 sin(\phi)$ as its output. Using the outputs of the two PSD's, the amplitude and phase of the control signal can be given as

$$
\begin{aligned}
Amplitude &= \sqrt[2]{V_{psd} + V_{psd2}} \\
Phase = &= tan^{-1}(\frac{V_{psd2}}{V_{psd}})
\end{aligned}
$$

Appendix C

Signal Averaging

Signal averaging is a technique used in signal processing to increase the signal-noise ratio (SNR). Assume a signal s(t) corrupted with noise n(t), uncorrelated with the signal. The signal power can be considered constant in the replicate measurements. The signal power S over a time T can be given as

$$S = \int_0^T E(s(t)^2)dt$$

Assuming the noise with zero mean and constant variance (σ) in the replicate measurements, the SNR is defined as

$$SNR = \frac{S}{\sigma^2}$$

Assuming $n_i(t)$ to be the noise signal for i^{th} averaging instant, the variance (σ_{avg}) of the signal after averaging N times is given by

$$\begin{aligned}
\sigma_{avg}^2 &= var(\frac{1}{N}\Sigma_{i=1}^N(n_i(t))) \\
&= \frac{1}{N^2} var\left(\Sigma_{i=1}^N(n_i(t))\right) \\
&= \frac{1}{N^2}\Sigma_{i=1}^N\left(var(n_i(t))\right) \\
&= \frac{1}{N}\sigma^2
\end{aligned}$$

The SNR after averaging can be given as

$$SNR_{avg} = \frac{S}{\sigma_{avg}^2} = N \times SNR$$

Bibliography

[1] M. S. Tamer, H. Sadeghian, A. Keyvani, J. F. L. Goosen, and F. van Keulen, "Quantitative measurement of tip-sample interaction forces in tapping mode atomic force microscopy,"

[2] A. Raman, S. Trigueros, A. Cartagena, A. Stevenson, M. Susilo, E. Nauman, and S. A. Contera, "Mapping nanomechanical properties of live cells using multi-harmonic atomic force microscopy," *Nature nanotechnology*, vol. 6, no. 12, pp. 809–814, 2011.

[3] R. Grover, B. McCarthy, D. Sarid, and I. Guven, "Mapping thermal conductivity using bimetallic atomic force microscopy probes," *Applied physics letters*, vol. 88, no. 23, p. 233501, 2006.

[4] H. H. Fang, K.-Y. Chan, and L.-C. Xu, "Quantification of bacterial adhesion forces using atomic force microscopy (afm)," *Journal of microbiological methods*, vol. 40, no. 1, pp. 89–97, 2000.

[5] J. Solon, I. Levental, K. Sengupta, P. C. Georges, and P. A. Janmey, "Fibroblast adaptation and stiffness matching to soft elastic substrates," *Biophysical journal*, vol. 93, no. 12, pp. 4453–4461, 2007.

[6] M. H. Richardson, "Modal mass, stiffness and damping," *Vibrant Technology, Inc., Jamestown*, pp. 1–5, 2000.

[7] T. R. RodrÄśÌĄguez and R. GarcÄśÌĄa, "Compositional mapping of surfaces in atomic force microscopy by excitation of the second normal mode of the microcantilever," *Applied Physics letters*, vol. 84, no. 3, 2003.

[8] R. Proksch, "Multifrequency, repulsive-mode amplitude-modulated atomic force microscopy," *Applied Physics letters*, vol. 89, no. 11, 2006.

[9] A. Keyvani, H. Sadeghian, M. S. Tamer, J. F. L. Goosen, and F. van Keulen, "Minimizing tip-sample forces and enhancing sensitivity in atomic force microscopy with dynamically compliant cantilevers," *Journal of Applied Physics*, vol. 121, no. 24, p. 244505, 2017.

[10] O. Sahin, C. F. Quate, and O. Solgaard, “Torsional harmonic cantilevers for detection of high frequency force components in atomic force microscopy,” Aug. 15 2006. US Patent 7,089,787.

[11] M. Sadeghian and J. KEYVANI, “Method of performing surface measurements on a surface of a sample, and scanning probe microscopy system therefore,” Apr. 27 2017. WO Patent App. PCT/NL2016/050,720.

[12] R. W. Stark and W. M. Heckl, “Fourier transformed atomic force microscopy: tapping mode atomic force microscopy beyond the hookian approximation,” *Surface Science*, vol. 457, no. 1, pp. 219–228, 2000.

[13] M. Verhaegen and P. Dewilde, “Subspace model identification part 1. the output-error state-space model identification class of algorithms,” *International journal of control*, vol. 56, no. 6, pp. 1187–1210, 1992.

[14] M. Verhaegen and P. Dewilde, “Subspace model identification part 2. the output-error state-space model identification class of algorithms,” *International journal of control*, vol. 56, no. 6, pp. 1211–1247, 1992.

[15] M. Verhaegen, “Subspace model identification part 3. the output-error state-space model identification class of algorithms,” *International journal of control*, vol. 58, no. 3, pp. 555–586, 1992.

[16] K. Abed-Meraim, W. Qiu, and Y. Hua, “Blind system identification,” *Proceedings of the IEEE*, vol. 85, no. 8, pp. 1310–1322, 1997.

[17] L. Tong, R.-W. Liu, V. C. Soon, and Y.-F. Huang, “Indeterminacy and identifiability of blind identification,” *IEEE Transactions on circuits and systems*, vol. 38, no. 5, pp. 499–509, 1991.

[18] L. Tong and S. Perreau, “Multichannel blind identification: From subspace to maximum likelihood methods,” *Proceedings of the IEEE*, vol. 86, no. 10, pp. 1951–1968, 1998.

[19] E.Meyer, “Atomic force microscopy.,” *Progress inSurface Science*, vol. 41, no. 1, pp. 3–49, 1992.

[20] T. Junno, K. Deppert, L. Montelius, and L. Samuelson, “Controlled manipulation of nanoparticles with an atomic force microscope,” *Applied Physics Letters*, vol. 66, no. 26, pp. 3627–3629, 1995.

[21] G. Binning, C. Quate, and C. Gerber, “Atomic force microscope.,” *Physical Review Letters*, vol. 56, no. 9, pp. 930–934, 1986.

[22] E.-L. Florin, V. T. Moy, H. E. Gaub, *et al.*, “Adhesion forces between individual ligand-receptor pairs,” *Science-AAAS-Weekly Paper Edition-including Guide to Scientific Information*, vol. 264, no. 5157, pp. 415–417, 1994.

[23] Keir.C.Neuman and A. Nagy, “Single-molecule force spectroscopy: optical tweezers, magnetic tweezers and atomic force microscopy,” *HHS Author Manuscript*, vol. 5, no. 6, pp. 491–505, 2008.

[24] B. Cappella and G. Dietler, "Force-distance curves by atomic force microscopy," *Surface Science Reports*, vol. 34, no. 1-3, pp. 1–103, 2012.

[25] D. Rugar and P. Hansma, "Atomic force microscopy," *Physics today*, vol. 43, no. 10, pp. 23–30, 1990.

[26] S. Sadewasser, "Experimental technique and working modes," in *Kelvin Probe Force Microscopy*, pp. 7–24, Springer, 2012.

[27] Q. Zhong, D. Innlss, K. Kjoller, and V. B. Ehngs, "Fractured polymer/silica fiber surface studied by tapping mode atomic force microscopy," *Surface Science Letters*, vol. 290, no. 1-2, pp. 688–692, 1993.

[28] D. Y. Abramovitch, S. B. Andersson, L. Y. Pao, and G. Schitter, "A tutorial on the mechanisms, dynamics, and control of atomic force microscopes," *American control conference*, pp. 3488–3502, 2007.

[29] Bruker Systems, "Introduction to bruker's scanasyst and peakforce tapping afm technology."

[30] O. Sahin, E. G. Yaralioglu, R. Grow, S. Zappe, A. Atalar, C. Quate, and O. Solgaard, "High-resolution imaging of elastic properties using harmonic cantilevers," *Sensors and actuators A : Physical*, vol. 114, no. 2, pp. 183–190, 2004.

[31] F. M. Sherry, K. Kjoller, J. T. Thornton, R. J. Tench, and D. Cook, "Electrical force microscopy, surface potential imaging, and surface electric modification with the atomic force microscope (afm)," *Bruker Systems.*

[32] A. Daniele, S. Salapaka, M. Salapaka, and M. Sahleh, "Piezoelectric scanners for atomic force microscopes: design of lateral sensors, identification and control," *American Control Conference, 1999. Proceedings of the 1999*, vol. 1, 1999.

[33] G. Schitter, P. Menold, H. F. Knapp, F. AllgÃűwer, and A. Stemme, "High performance feedback for fast scanning atomic force microscopes," *Review of Scientific Instruments*, vol. 72, no. 8, 1999.

[34] B. Peters and G. D. Roeck, "Reference-based stochastic subspace identification for output-only modal analysis," *Mechanical Systems and Signal Processing*, vol. 13, no. 6, pp. 855–878, 1999.

[35] L. Tong, R.-W. Liu, V. C. Soon, and Y.-F. Huang, "Indeterminacy and identifiability of blind identification," *IEEE Transactions on circuits and systems*, vol. 38, no. 5, pp. 499–509, 1991.

[36] C. Sanathanan and J. Koerner, "Transfer function synthesis as a ratio of two complex polynomials," *IEEE transactions on automatic control*, vol. 8, no. 1, pp. 56–58, 1963.

[37] J. Buchholz and W. v. Grünhagen, "Inversion impossible?," 2007.

[38] E. Levy, "Complex-curve fitting," *IRE transactions on automatic control*, no. 1, pp. 37–43, 1959.

[39] R. Levy and M. Maaloum, “Measuring the spring constant of atomic force microscope cantilevers: thermal fluctuations and other methods,” *Nanotechnology*, vol. 13, no. 1, p. 33, 2001.

[40] J. L. Hutter and J. Bechhoefer, “Calibration of atomic-force microscope tips,” *Review of Scientific Instruments*, vol. 64, no. 7, pp. 1868–1873, 1993.

[41] Wikibooks, “Nanotechnology — wikibooks, the free textbook project,” 2013.

[42] J. H. Scofield, “Frequency domain description of a lock-in amplifier,” *American journal of physics*, vol. 62, no. 2, pp. 129–132, 1994.